


## Extreme-mass-ratio inspirals into rotating boson stars: Nonintegrability, chaos, and transient resonances

Kyriakos Destounis<sup>1</sup>, Federico Angeloni<sup>2</sup>, Massimo Vaglio<sup>3</sup>, and Paolo Pani

*Dipartimento di Fisica, Sapienza Università di Roma, Piazzale Aldo Moro 5, 00185, Roma, Italy  
and INFN, Sezione di Roma, Piazzale Aldo Moro 2, 00185, Roma, Italy*

 (Received 12 May 2023; accepted 2 October 2023; published 30 October 2023)

General relativity predicts that black holes are described by the Kerr metric, which has integrable geodesics. This property is crucial to produce accurate waveforms from extreme-mass-ratio inspirals. Astrophysical environments, modifications of gravity, and new fundamental fields may lead to non-integrable geodesics, inducing chaotic effects. We study geodesics around self-interacting rotating boson stars and find robust evidence of nonintegrability and chaos. We identify islands of stability around resonant orbits, where the orbital radial and polar oscillation frequency ratios, known as rotation numbers, remain constant throughout the island. These islands are generically present in both the exterior and the interior of compact boson stars. A monotonicity change of rotation curves takes place as orbits travel from the exterior to the interior of the star. Therefore, configurations with neutron-star-like compactness can support degenerate resonant islands. This anomaly is reported here for the first time, and it is not present in black holes. Such configurations can also support extremely prolonged resonant islands that span from the exterior to the interior of the star and are shielded by thick chaotic layers. We adiabatically evolve inspirals using approximated post-Newtonian fluxes and find time-dependent plateaus in the rotation curves which are associated with island-crossing orbits. Crossings of external islands give rise to typical gravitational-wave glitches found in non-Kerr objects. Furthermore, when an inspiral is traversing an internal island that is surrounded by a thick chaotic layer, a new type of simultaneous multifrequency glitch occurs that may be detectable with space interferometers such as the Laser Interferometer Space Antenna and can serve as evidence of an extreme-mass-ratio inspiral around a supermassive boson star.

DOI: [10.1103/PhysRevD.108.084062](https://doi.org/10.1103/PhysRevD.108.084062)

### I. INTRODUCTION

Ground-based gravitational-wave (GW) interferometers are about to start a new observation run and will continue detecting GW signals from the coalescence of compact binaries [1–3] and possibly from other GW sources in the years to come. To date, almost a hundred compact binary mergers have been reported. Despite the fact that the majority of events are well understood as either black-hole (BH) or neutron-star (NS) or mixed BH-NS mergers, some puzzling “mass-gap” events, such as GW190814 [4] and GW190521 [5,6], challenge standard formation scenarios and have motivated exotic alternatives (see, e.g., [7]). With the GW event catalog ever increasing, the possibility of detecting exotic compact objects (ECOs) other than BHs and NSs is worth exploring [8,9].

We are now convinced that an important amount of nonluminous exotic matter, known as dark matter [10–12], is paramount in the formation [13] and amalgamation of galaxies [14] as well as in determining the earliest, current, and future state of the Universe [13,15–19]. This raises the possibility of new fundamental particles comprising the missing cosmological mass. With scalar fields predominantly used to model early Universe physics, the case arises

that such fields could form equilibrium condensates, held together by their own gravity, through a mechanism known as gravitational cooling [20,21]. Such prototypical class of ECOs has been dubbed boson stars (BSs), and their conceptualization dates back to the late 1960s [22–25] and 1980s [26–33].

At the fundamental level, BSs are the simplest localized configurations of a complex scalar field, governed by classical equations; thus, even if they have not yet been observed in nature, they still can serve as models for compact objects ranging from particles to stars and less dense galactic halos. In all these cases, BSs are endowed with a balance between the dispersive nature of scalar matter and the gravitational pull holding them together (see [34–36] for reviews on various types of BSs). BSs do not have an event horizon nor a singularity, are asymptotically flat, and may exhibit stable light rings, isolated ergoregions, and superextremal spins, which can lead to new GW phenomenology [36–42]. As a consequence, they are considered among the best models of ECOs and a proxy to test the nature of compact objects in the extreme-gravity regime [8,43–45]. Another important motivation concerns the fact that BSs (and their real-scalar counterparts,

known as oscillons [46]) could form in the early Universe [47,48] from large overdensities, being, thus, (meta)stable relics of inflation [49,50] and compelling dark-matter candidates [51,52].

Static BS configurations are linearly stable to perturbations [38,40,53–57] and can consistently form dynamically from diffuse initial states [33,58–61] as well as from collisions and binary mergers [7,62–73]. On the other hand, spinning BSs were found to be unstable toward a bar-mode instability [21,74], unless scalar self-interaction terms in the model are sufficiently strong [75]. This instability is not present for rotating BSs made by a massive vector field [74].

To date, a variety of bosonic potentials have been considered [26,27,76–83], each one providing a different relation between the BS maximum mass and the underlying field-theory parameters. As a rule of thumb, strong self-interactions can make the maximum mass parametrically larger than in the free-scalar case, motivating alternative models for supermassive objects in galactic cores, which can mimic the shadows [84–89] and particle orbits around ordinary BHs [38,90].

Hence, it is of utmost importance to devise further tests in order to distinguish BSs through orbital dynamics and GW observations. In this work, we focus on extreme-mass-ratio inspirals (EMRIs), consisting of a primary supermassive compact object (which we assume to be a self-interacting, compact, spinning BS) and a stellar-mass compact secondary. So far, geodesic and inspiral studies have been carried out at the equatorial plane of nonrotating [37–39,91–93] and rotating BSs [94–96] (see also the recent [97] for circular, equatorial EMRIs around hairy BHs [98] interpolating between a Kerr BH and a BS without self-interactions). The emitted GWs during circular equatorial geodesics and EMRIs were also analyzed in some BS models [37,38,97,99,100]. However, a geodesic and inspiral analysis is lacking for generic, nonequatorial and noncircular, trajectories around spinning BSs. Generic orbits not only will help to further constrain the existence of supermassive BSs through their considerably more intricate waveform signal, but are also tools to examine the integrability of the underlying geodesic equations that govern particle motion. If geodesics around BSs are integrable, then the evolution is regular and no chaotic phenomena are present, as in the Kerr case. In this case, geodesics and EMRIs between rotating BSs and Kerr BHs will differ only by their different multipolar structure [44,45,101–104]. Alternatively, if geodesics around rotating BSs break integrability, then direct and indirect chaotic imprints emerge that are clearly distinguishable at both the orbital [105–116] and GW level [117–119].

It is the main goal of this work to study generic orbits and EMRIs around supermassive self-interacting BSs in order to assess if their exotic multipolar structure [44,45,101–104] breaks integrability and gives rise to imprints of chaos.

If geodesics around such objects are nonintegrable, then GW observations from future space-borne detectors like the Laser Interferometer Space Antenna (LISA) [120–125], TianQin [126], and Taiji [127,128] may lead to distinguishable effects that can break the degeneracy between supermassive BHs and BSs in galactic centers.<sup>1</sup> In what follows, we adopt geometrized units so that  $G = c = 1$ .

## II. GEODESICS AND CHAOS

Generic stationary and axisymmetric spacetimes can be written as

$$ds^2 = g_{tt}dt^2 + 2g_{t\varphi}dtd\varphi + g_{rr}dr^2 + g_{\theta\theta}d\theta^2 + g_{\varphi\varphi}d\varphi^2, \quad (1)$$

where the metric tensor components are, in general, functions of  $r$  and  $\theta$  and the coordinate system  $(t, r, \theta, \varphi)$  can be, e.g., of Boyer-Lindquist type [130] or quasi-isotropic [131]. The motion of a secondary point particle orbiting the spacetime geometry of the primary compact object [as defined by Eq. (1)] is described by the geodesic equations

$$\ddot{x}^\kappa + \Gamma_{\lambda\nu}^\kappa \dot{x}^\lambda \dot{x}^\nu = 0, \quad (2)$$

where  $\Gamma_{\lambda\nu}^\kappa$  are the Christoffel symbols of spacetime,  $x^\kappa$  is the four-position vector of the orbit, and the overdots denote differentiation with respect to proper time  $\tau$ . The geodesic equation (2) breaks down into four equations of motion, one for each coordinate component of the particle's trajectory,  $x^\kappa(\tau)$ . This system of second-order, coupled differential equations can be considerably simplified using spacetime symmetries. The spacetime (1) assumed in this work possesses two Killing vector fields resulting from stationarity and axisymmetry (the metric tensor is  $t$  and  $\varphi$  independent), yielding two conserved quantities throughout geodesic motion, i.e., the specific energy and  $z$  component of the angular momentum of the particle:

$$-E/m = g_{tt}\dot{t} + g_{t\varphi}\dot{\varphi}, \quad L_z/m = g_{t\varphi}\dot{t} + g_{\varphi\varphi}\dot{\varphi}, \quad (3)$$

where  $m$  is the mass of the orbiting particle. Rearranging Eq. (3), we obtain two first-order, decoupled differential equations for the  $t$  and  $\varphi$  momenta as

$$\dot{t} = \frac{Eg_{\varphi\varphi} + L_zg_{t\varphi}}{m(g_{t\varphi}^2 - g_{tt}g_{\varphi\varphi})}, \quad \dot{\varphi} = \frac{Eg_{t\varphi} + L_zg_{tt}}{m(g_{tt}g_{\varphi\varphi} - g_{t\varphi}^2)}, \quad (4)$$

which can be solved once  $r(\tau)$  and  $\theta(\tau)$  are known. The two remaining equations of motion for  $r$  and  $\theta$  are, in general, coupled and of second differential order. Test particles in

<sup>1</sup>Note that also EMRIs around stellar-mass compact objects would be potentially detectable by third-generation detectors such as the Einstein Telescope if the secondary is a subsolar compact object [129].

geodesic motion provide a third constant of motion, namely, the conservation of their rest mass (or, equivalently, their four-velocity  $g_{\lambda\nu}\dot{x}^\lambda\dot{x}^\nu = -1$ ), which leads to a constraint equation of the form

$$\dot{r}^2 + \frac{g_{\theta\theta}}{g_{rr}}\dot{\theta}^2 + V_{\text{eff}} = 0, \quad (5)$$

with  $V_{\text{eff}}$  being a Newtonian-like potential:

$$V_{\text{eff}} \equiv \frac{1}{g_{rr}} \left( 1 + \frac{g_{\varphi\varphi}E^2 + g_{tt}L_z^2 + 2g_{t\varphi}EL_z}{m^2(g_{tt}g_{\varphi\varphi} - g_{t\varphi}^2)} \right) \quad (6)$$

that characterizes bound geodesic motion. When  $V_{\text{eff}} = 0$ , the resulting curve is called the curve of zero velocity (CZV), since  $\dot{r} = \dot{\theta} = 0$  there.

If a hypothetical rank-two (or higher-rank) Killing tensor field exists, then the motion of  $r(\tau)$  and  $\theta(\tau)$  decouples into first-order differential equations. A special case where a rank-two Killing tensor exists is the Kerr solution where the role of the separation constant is played by the famous Carter constant [132]. However, since the compact object we will assume throughout our analysis has a different multipolar structure than that of a Kerr BH (and, furthermore, it is known only numerically), it is unlikely that a separation, Carter-like, constant (or any other higher-rank Killing tensor) exists. Thus, to evolve orbits, we will use the coupled second-order differential equation system for  $r$  and  $\theta$ , together with Eqs. (4) and (5), without any further symmetry assumptions besides stationarity and axisymmetry.

The existence of Carter's separation constant not only is a useful tool to evolve trajectories in Kerr spacetime faster, but rather implies an important aspect of geodesics, namely, their integrability. Kerr spacetimes have four degrees of freedom. Stationarity and axisymmetry lead to the reduction of degrees of freedom to two. Taking into account the existence of the Carter constant and the conservation of the rest mass of the test particle reduces the degrees of freedom of orbital motion to zero; geodesics around Kerr BHs are integrable and do not present chaotic features [105,106,108,111,112,117–119,133]. Unfortunately, Carter's symmetry is extremely fragile and in many occasions is broken by simply deforming the multipolar structure of spacetime by considering accretion disks and BH environments [134–140], modifications of gravity [112,113], neutron stars [141–144], exotic compact objects [145,146], or in a parametrized way by introducing agnostic deformations to Kerr—a class of metrics called bumpy or non-Kerr BHs [147–158]. In these cases, the integrability property may be broken, leading to chaotic effects [133]. Full-blown, ergodic chaos is not expected to occur in astrophysical scenarios, such as EMRIs, but nonintegrabilitylike effects are anticipated even when geodesics are

integrable [159–162] due to dissipation. This is mainly due to the manifestation occurring around transient orbital resonances which are expected to affect EMRI evolution and parameter estimation, though nonintegrable EMRIs are even more likely to amplify these effects and can introduce clear chaotic phenomena [105–108,108–111,117–119]. A generic orbit of an integrable system can be described by its revolution frequency  $\omega_\varphi$  and two librationlike frequencies: the frequency of oscillation from the periapsis to the apoapsis and back,  $\omega_r$ , and the oscillation frequency through the equatorial plane,  $\omega_\theta$ . Generic orbits possess irrational ratios of the above frequencies and these orbits fill densely the available phase space of a three-dimensional torus. On the other hand, resonant (periodic) orbits have commensurate (rational) ratios of orbital frequencies, which means that the particular orbits are returning to their initial position after some revolutions depending on their periodicity; thus, they are not phase-space filling. When orbital resonances are encountered during inspirals of equal mass binaries, e.g., in the kilohertz band of LIGO/Virgo/KAGRA detectors, they do not affect the evolution, since the inspiral is extremely rapid. However, when the binary is highly asymmetric, i.e., an EMRI, then the adiabatic nature of the secondary's motion can experience orbital resonances for a significant number of cycles and lead to substantial effects, such as cumulative dephasing and putative erroneous parameter estimation [159–161].

When a nonintegrable perturbation is introduced to the system, two theorems, namely, the Kolmogorov-Arnold-Moser (KAM) [163,164] and Poincaré-Birkhoff [165] theorems, dictate how the phase-space structure is altered around resonant points. KAM theorem ensures that, when the orbits are sufficiently away from resonances, the system behaves as if it were integrable. The trajectories in the phase space lie on a torus defined by the integrals of motion and successive intersections of the orbits on a perpendicular two-dimensional surface (the Poincaré surface of section) form curves that organize around a common, fixed, central point. These are called KAM curves and the whole structure is known as a Poincaré map, whose central point corresponds to a planar circular orbit. Close to periodic orbits, the KAM curves disintegrate into two sets of periodic points in the Poincaré map, in accord with the Poincaré-Birkhoff theorem: the stable ones which are surrounded by islands of stability (resonant islands) and the unstable ones where chaotic orbits emanate and surround the islands of stability with thin layers. The whole structure around resonances of nonintegrable systems is called a Birkhoff chain (see Fig. 2 in [106] for an illustration). The crucial aspect of resonant islands, and their significance in EMRIs, is the fact that the rational ratio of the orbital frequencies  $\omega_r/\omega_\theta$  is shared throughout the island for all geodesics that occupy it. Put in other words, integrable EMRIs experience resonances that occupy a



zero-volume point in phase space, while nonintegrable EMRIs exhibit prolonged resonances where the secondary is locked in perfect resonance for a rather significant amount of revolutions (order of a few hundreds of cycles, for typical mass ratios and depending on the non-Kerr object [106,111,117–119]) without taking into account pre- and postresonant effects [166] and conservative effects from gravitational self-force [167] which are essential for integrable EMRIs to show signs of transient resonant phenomena.

The existence of ergodic chaos and islands of stability around periodic points are direct and indirect signatures of nonintegrability, respectively; therefore, sketching a detailed Poincaré map can unravel if the system under study is chaotic. When the perturbation introduces a slight nonintegrable deformation to the system, there are other techniques to assess if and at which initial conditions of geodesics the aforementioned phenomena manifest themselves. The rotation number is one of the most helpful tools to find regions of interest in order to search for islands of stability. We calculate it by tracking the angle  $\vartheta$  between successive intersections on KAM curves, relative to the fixed central point of the Poincaré map. The rotation number is defined as the summation of all angles  $\vartheta$  measured between consecutive intersections, i.e., [133]

$$\nu_\vartheta = \frac{1}{2\pi N} \sum_{i=1}^N \vartheta_i, \quad (7)$$

where  $N$  is the number of angles measured. When  $N \rightarrow \infty$ , Eq. (7) asymptotes to the orbital frequency ratio  $\nu_\vartheta = \omega_r/\omega_\theta$ . Calculating consecutive rotation numbers for different initial conditions of orbits, by smoothly varying one of the parameters of the system while keeping the rest fixed, leads to a rotation curve.

Integrable systems show monotonic rotation curves, while nonintegrable systems display discontinuities in the monotonicity through the formation of transient plateaus with a nonzero width when geodesics transverse resonant islands. Inflection points can also appear when trajectories pass through unstable periodic points. Nevertheless, by changing the initial conditions properly, the orbit can be driven through the island and give rise to a plateau. So far, all studies have dealt with compact objects that are either non-Kerr or bumpy in nature and either possess an event horizon or have serious causal structure pathologies. In the following sections, we will examine the characteristic features of rotating self-interacting BSs with geodesics and approximate EMRI evolutions in order to first assess whether geodesic motion in such spacetimes is nonintegrable and, then, to establish various phenomenological imprints of chaos in the associated GW signal.

Before we proceed, we note that all numerical evolution have been performed with respect to the inertial time of the detector at infinity and not with respect to proper time in

order to extract the corresponding GW emission of EMRIs. To achieve that, we have transformed the equations of motion from proper to inertial time by the use of the chain rule for first and second derivatives with respect to proper time, e.g.,  $\dot{r} = dr/d\tau = (dr/dt)(dt/d\tau) = ir'$ , where we have defined  $r' \equiv dr/dt = \dot{r}/i$ . Equivalent equations hold for  $\theta$ ,  $\varphi$ , and  $t$  as well as for the constraint equation (5).

### III. SELF-INTERACTING ROTATING BSs

The equilibrium configurations of rotating BSs can be constructed starting from the globally  $U(1)$ -invariant action

$$S = \int d^4x \sqrt{-g} \left[ \frac{R}{16\pi} - \mathcal{L}_\phi \right], \quad (8)$$

which describes the dynamics of a complex, massive scalar field  $\phi$ , minimally coupled to gravity. The Lagrangian  $\mathcal{L}_\phi$  considered in this work is characterized by a mass parameter  $\mu$ , plus quartic repulsive corrections, controlled by the coupling  $\lambda$ , which add linearly to the kinetic term as

$$\mathcal{L}_\phi = -\frac{1}{2} g^{\alpha\beta} \phi_{,\alpha}^* \phi_{,\beta} - \frac{1}{2} \mu^2 |\phi|^2 - \frac{1}{4} \lambda |\phi|^4. \quad (9)$$

The requirement of stationarity and axisymmetry leads to the following ansatz for the scalar field:

$$\phi = \phi_0(r, \theta) e^{i(s\varphi - \Omega t)}, \quad (10)$$

where  $\Omega > 0$  is the field's angular frequency, which determines the phase evolution in time, while  $s$  is an integer called the azimuthal (or rotational) winding number and can be proven to correspond to the ratio between the conserved angular momentum and particle number [35,168,169]. The ansatz (10) ensures that the stress-energy tensor  $T_{\alpha\beta}[g^{\alpha\beta}, \phi, \partial_\alpha \phi]$  does not depend on  $t$  and  $\varphi$  and sources a spacetime metric with time and azimuthal symmetry.

In this work, following [101,104], we consider spinning BSs with large self-interactions, i.e., characterized by  $\lambda/\mu^2 \gg 1$ . In this limit, the  $(r, \theta)$  scalar profile is approximately constant in the star's interior, and one can neglect the radial and polar derivatives of the field ( $\partial_r \phi \sim 0$ ,  $\partial_\theta \phi \sim 0$ ) while assuming  $\phi \sim 0$  in the exterior. This allows expressing the stress-energy tensor of the BS as that of a perfect fluid and to define the radius as in ordinary stars.<sup>2</sup> Furthermore, with an appropriate redefinition of the

<sup>2</sup>In the general case, the stress-energy tensor of a BS contains anisotropic terms and the scalar field, although exponentially decreasing, extends up to infinity, so that the radius is conventionally defined as the value of the radial coordinate enclosing a sufficiently large fraction (typically 99%) of the total mass [24,25,170]. In our case, instead, the scalar field has compact support and the radius is uniquely defined.

variables and parameters, the coupling constants in the Lagrangian can be factored out, so that each numerical solution corresponds to a one-parameter family of configurations, controlled by the effective mass parameter  $M_B = \sqrt{\lambda}/\mu^2$  [104]. The dimensionful physical quantities characterizing each BS, such as its mass, radius, and energy density, can be obtained from the dimensionless ones, characterizing each numerical solution, by multiplying them by the required power of  $M_B$  to match their dimension in mass and scale correspondingly as it changes.

Adopting quasi-isotropic coordinates, the line element (1) can be described through four independent functions  $(\rho, \gamma, \omega, \alpha)$  of  $(r, \theta)$  as

$$g_{tt}(r, \theta) = -e^{\gamma(r, \theta) + \rho(r, \theta)} + \omega(r, \theta)^2 e^{\gamma(r, \theta) - \rho(r, \theta)} r^2 \sin^2 \theta, \quad (11a)$$

$$g_{rr}(r, \theta) = \frac{g_{\theta\theta}(r, \theta)}{r^2} = e^{2\alpha(r, \theta)}, \quad (11b)$$

$$g_{t\varphi}(r, \theta) = -\omega(r, \theta) e^{\gamma(r, \theta) - \rho(r, \theta)} r^2 \sin^2 \theta, \quad (11c)$$

$$g_{\varphi\varphi}(r, \theta) = e^{\gamma(r, \theta) - \rho(r, \theta)} r^2 \sin^2 \theta. \quad (11d)$$

We constructed the solutions numerically following the method described in [56,104] which makes use of an integral representation of the Einstein equations to set up an iterative integration scheme. The algorithm starts with a solution corresponding to a nonrotating BS defined on a two-dimensional grid of  $r \in (10^{-6}, 10)M_B$  [which typically corresponds to  $r \in (10^{-5}, 100)M$  in terms of the BS mass  $M$ ],  $\theta \in (0, \pi/2)$ , and converges to a spinning configuration, close to the initial one, within roughly 150 iterations, with a relative error of  $\mathcal{O}(10^{-4})\%$  for all metric functions and the scalar profile. The details of the numerical implementation are provided in [104].

The maximum mass that can be reached by these stars scales as [26,104]

$$M_{\max} \sim \gamma(\chi) M_B = \gamma(\chi) \frac{\sqrt{\lambda \hbar}}{m_s^2} M_p^3, \quad (12)$$

where  $m_s = \mu \hbar$  is the mass of the boson,  $M_p$  is the Planck mass, and  $\gamma(\chi)$  is a  $\mathcal{O}(0.1)$  factor which depends on the dimensionless spin  $\chi = J/M^2$  (where  $J$  is the angular momentum of the solution). This means, for instance, that, for  $\lambda \hbar \sim \mathcal{O}(10^{-80})$  and  $m_s$  in the range  $10^{-15} - 10^{-12}$  eV, the model allows for compact stellar configurations with  $M_{\max}$  in the range  $10 - 10^7 M_\odot$ . For  $\lambda$  as large as  $\lambda \sim \mathcal{O}(\hbar^{-1})$ , the same range of  $M_{\max}$  corresponds to  $m_s \in (0.1, 100)$  MeV.

In what follows, we consider rapidly rotating supermassive configurations with  $\chi \sim 0.8$ , the same mass, and decreasing compactness, whose properties are listed in

TABLE I. Self-interacting, rotating BSs considered in this work. The three configurations have the same dimensionless spin and mass but different compactnesses and frequencies (due to the different effective coupling  $M_B$ ). The compactness is defined by  $\mathcal{C} \equiv M/R$ , where  $R$  is the star's perimeteral radius [172]. The order of magnitude chosen for  $M_B$  corresponds, considering  $\lambda/\mu^2 \sim \mathcal{O}(100) \gg 1$ , to a mass of the boson  $m_s = \hbar\mu \sim 10^{-14}$  eV.

	$M/M_\odot$	$\chi$	$\mathcal{C}$	$\Omega$	$M_B/M_\odot$
Case 1	$10^6$	0.8	0.25	0.73	$8.5 \times 10^6$
Case 2	$10^6$	0.8	0.19	0.80	$9.0 \times 10^6$
Case 3	$10^6$	0.8	0.16	0.82	$1.0 \times 10^7$

Table I. All the configurations have topological genus 1 [104], at variance with their vector counterparts, spinning Proca stars [171], which have instead a spherical topology even when spinning.

The configuration of case 1 is the most compact one and corresponds to the maximum-mass solution for  $\chi = 0.8$ . A comparison with the Kerr solution, sharing the same mass and spin, is shown in Fig. 1, in terms of the functions  $U_{tt} \equiv (g_{tt} + 1)/2$  and  $U_{rr} \equiv (g_{rr} - 1)/2$  evaluated on the equatorial plane. The corresponding Kerr event horizon and BS radius are also shown as well as the Newtonian gravitational potential  $M/r$  for an object of the same mass.

All the configurations in Table I are in a linearly perturbative stable branch of the mass-frequency diagram.

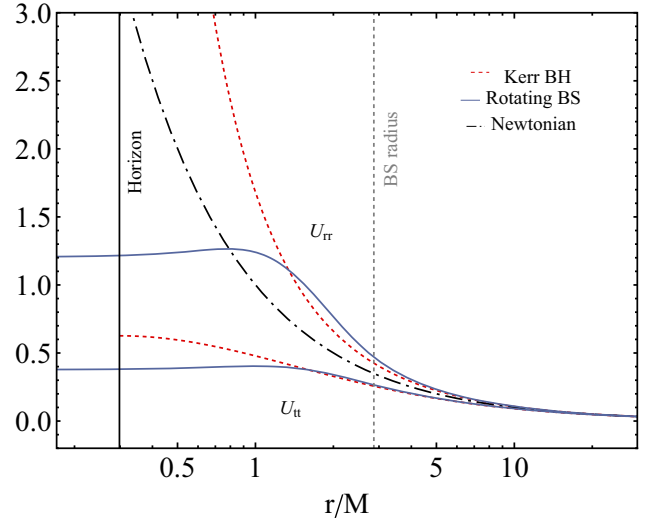


FIG. 1. Comparison between the Newtonian potential  $M/r$  (black dashed line) and the equatorial radial profiles of  $U_{tt} \equiv (g_{tt} + 1)/2$  and  $U_{rr} \equiv (g_{rr} - 1)/2$  for the Kerr metric (red dashed line) and the rotating BS (blue solid line) corresponding to case 1. The black solid and gray dashed vertical lines correspond to the location of the Kerr horizon and the BS radius in the quasi-isotropic radial variable  $r/M$ .

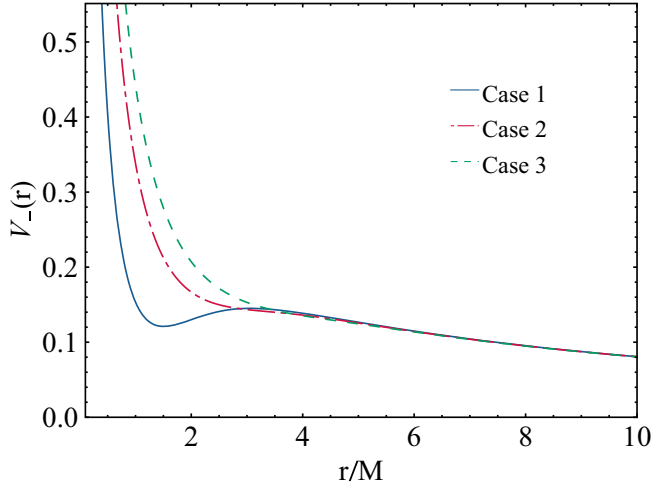


FIG. 2. Equatorial effective potentials  $V_-(r)$  for the BS configurations corresponding to our three case studies. The BS in case 1 has two light rings, corresponding to the stationary points  $V'_-(r) = 0$ , one of which is unstable and outside the star, while the other is stable and inside it. Stationary points of  $V_-(r)$  correspond to counterrotating circular photon orbits, while  $V_+$  (not shown here) is associated to corotating photon orbits which are not present for these configurations.

It is known that BSs with no or weak self-interactions are subject to a dynamical nonaxisymmetric instability that develops on short timescales [21]. Such instability has been shown to be quenched if the scalar self-interactions are sufficiently strong [75]. This is precisely the limit in which our solutions are obtained, with the explicit value of  $\lambda/\mu^2$  depending on the individual choices for  $\lambda$  and  $\mu$ , once  $M_B$  is fixed. Rotating BSs in this regime have also recently been formed dynamically in numerical simulations as a result of a binary coalescence, starting from nonrotating components in a quasicircular orbit [73].

Another source of instability is potentially linked to the presence of light rings. It has been recently shown [173] that exotic ultracompact objects, i.e., compact objects

featuring a light ring [8], are unstable under nonlinear perturbations due to the presence of a stable photon orbit in their interior, which traps massless perturbation modes [155]. Light rings are found as stationary points of the effective potentials

$$V_{\pm} \propto \frac{-g_{t\phi} \pm \sqrt{g_{t\phi}^2 - g_{tt}g_{\phi\phi}}}{g_{\phi\phi}}, \quad (13)$$

where the plus (minus) sign corresponds to orbits that are corotating (counterrotating) with the star. Among our three configurations, only case 1 exhibits a pair of light rings (one stable and one unstable) in the effective potential for counterrotating orbits  $V_-$ , as depicted in Fig. 2. Although this likely makes this configuration prone to instability—through either migration to a stable nonultracompact configuration or collapse into a BH—the timescale of such instability is unknown due to the absence of simulations for these particular BS models. Furthermore, the frequency of the star is close to the critical frequency for which no light rings are featured, corresponding to an infinite timescale. For these reasons, we chose to keep this solution as an example of high-compactness spinning BS. In any case, stable configurations near case 1 are expected to have similar geodesic properties.

For completeness, in Fig. 3, we present the meridional section of the energy density of the rotating BS cases considered, where the relative compactness and star radii are evident. All energy densities have been normalized with respect to the maximum value reached by case 1.

#### IV. GEODESIC ANALYSIS OF GENERIC ORBITS

Before embarking into the discussion of the results obtained through geodesic evolutions of orbits around rotating BSs, we report that the metric tensor components of our three configurations have been constructed with

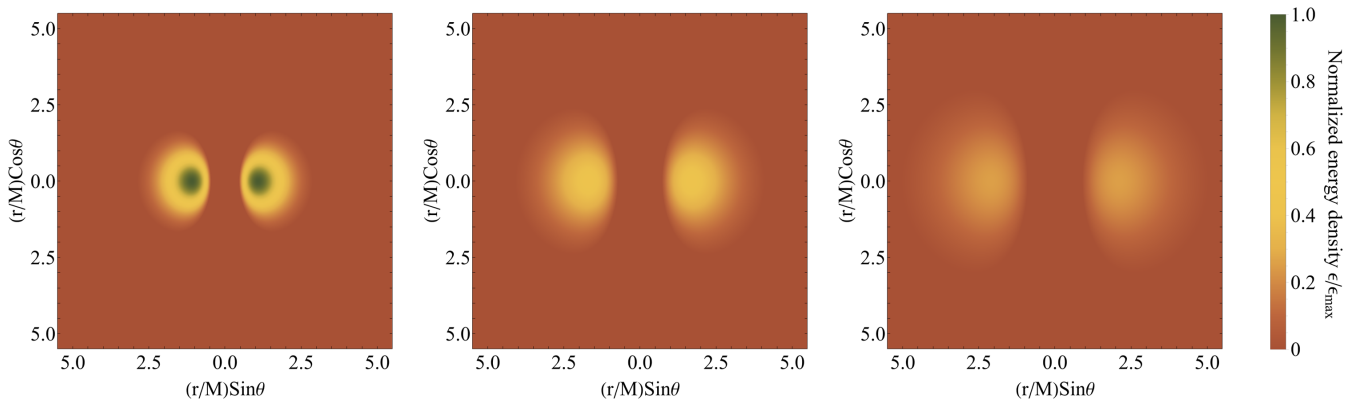


FIG. 3. Meridional section showing the energy density distribution  $\epsilon$  of our representative BSs (from left to right with decreasing compactness: cases 1, 2, and 3), normalized to the largest value  $\epsilon_{\max}$  (attained in case 1).

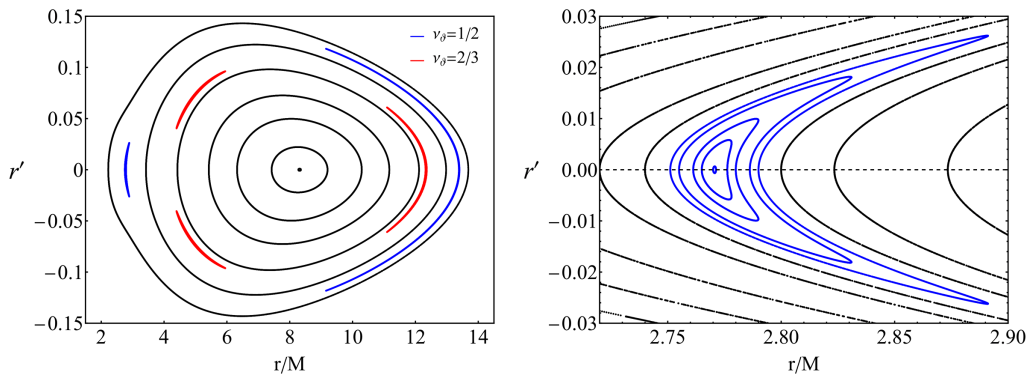


FIG. 4. Left: Poincaré map of a secondary with  $m = 1M_{\odot}$  orbiting around a compact rotating BS with  $M = 10^6 M_{\odot}$  and  $C = 0.25$  while the rest of the configuration quantities are stated in Table I (case 1). The secondary's conserved energy and angular momentum are  $E/m = 0.95$  and  $L_z/m = 3M$ , respectively. The fixed initial conditions chosen here are  $\dot{r}(0) = 0$  and  $\theta(0) = \pi/2$ , and  $\dot{\theta}(0)$  is defined by the constraint equation to guarantee bound motion while  $r(0)$  is varied. Black curves that surround the central fixed point of the map designate intersections of generic orbits through the equatorial plane, with different initial  $r(0)$ , while colored curves designate intersections that belong to different resonant islands of stability. Right: enlargement of the leftmost region where the  $1/2$  island of stability resides. Similar encapsulated structure is found for the rest of the islands.

varying number of grid points on the  $r$  and  $\theta$  coordinates to test convergence. The islands of stability and corresponding plateau widths at resonance in rotation curves reported below converge to  $\lesssim 1\%$  as we increased the number of grid points from  $300 \times 200$  to  $1000 \times 700$ . Interestingly, the island and plateau widths converge from below, meaning that more grid points lead to slightly larger islands till convergence occurs, which guarantees their existence regardless of the grid resolution and, therefore, ensures nonintegrability. For all simulations presented herein, we find that the constraint equation (5) is satisfied to within one part in  $10^8$  for the first 5000–10,000 revolutions (and intersections through the equatorial plane, depending on the initial conditions and BS configuration).

Finally, in all cases, we fix the mass ratio of the EMRI to  $m/M = 10^{-6}$  and choose the initial energy and  $z$  component of the angular momentum as  $E/m = 0.95$  and  $L_z/m = 3M$ , respectively.

### A. Case 1

Case 1 is a representative example for a compact spinning BS. The Poincaré map shown in Fig. 4 clearly shows that rotating BSs with large compactness are non-integrable, since around resonances such as  $\nu_{\theta} = 1/2, 2/3$  islands of stability form that encapsulate stable periodic points of geodesics.

From the maps, we calculate the rotation curves for two different choices of initial radial velocity, one with  $\dot{r}(0) = r'(0) = 0$  and one with  $\dot{r}(0) = 0.1$ , shown in Fig. 5. The rotation curves for this configuration looks quite similar to those found in [106,112,119], i.e., an inflection point around the  $2/3$  resonance and a plateau at  $1/2$  resonance when  $\dot{r}(0) = 0$ . The absence of an event horizon allows for bound geodesics even inside the BS, with its radius designated with a vertical dashed line, surprisingly next to where the  $1/2$  plateau resides. Therefore, the first non-BH feature is the existence of resonant islands even inside

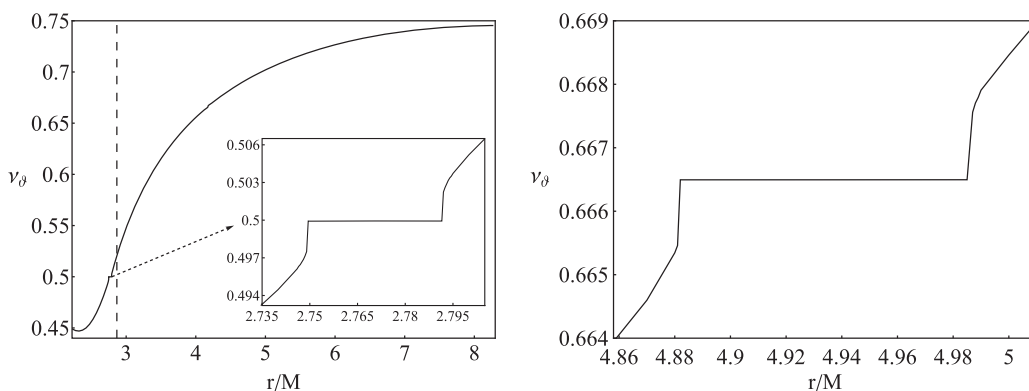


FIG. 5. Left: rotation curve corresponding to the same system as in Fig. 4. The vertical dashed line represents the radius of the BS, while the inset enlarges the surrounding region of the  $1/2$  plateau. Right: the same as in the left panel but with  $\dot{r}(0) = 0.1$ . The initial velocity gives access to the  $2/3$  island of stability.



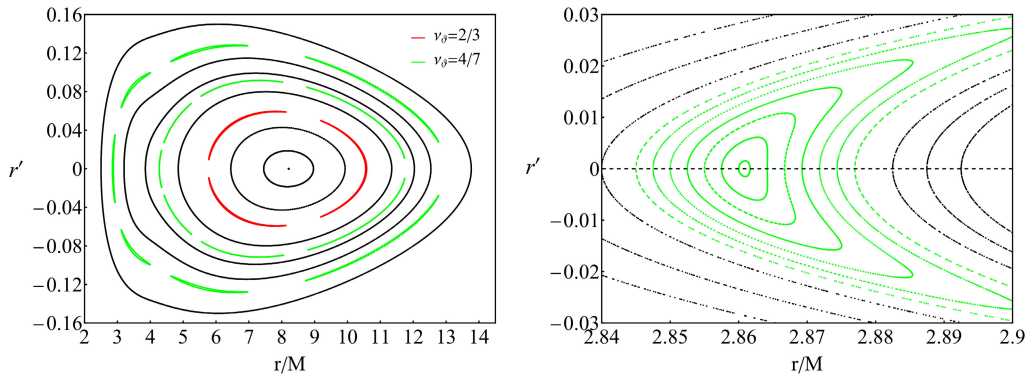


FIG. 6. Left: the same as in Fig. 4 but for case 2 (intermediate compactness  $\mathcal{C} = 0.19$ ). Right: enlargement of the leftmost region where the 4/7 island of stability resides. Similar encapsulated structure is found for the rest of the islands.

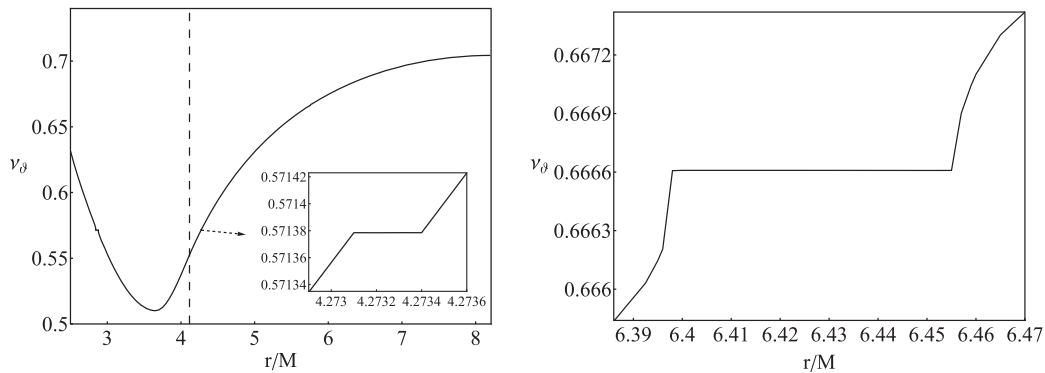


FIG. 7. Left: rotation curve corresponding to the same system as in Fig. 5. The horizontal dashed line represents the radius of the BS, while the inset enlarges the surrounding region of the external 4/7 plateau. Right: the same as in the left panel but with  $\dot{r}(0) = 0.058$ . The initial velocity gives access to the 2/3 island of stability.

the star. Another interesting feature is the change in monotonicity close to plunge<sup>3</sup> for case 1, which has also been observed for Kerr BHs with soft scalar hair and BSs in the study of epicyclic frequencies [174]. The inflection point at rotation number 2/3 for  $\dot{r}(0) = 0$ , in the left panel in Fig. 5, designates the passage of an orbit between two edges of resonant islands, where there is an unstable periodic point. Changing the initial radial velocity to  $\dot{r}(0) = 0.1$ , as we show for the rotation curve in Fig. 5 (right panel), the phase-space trajectory crosses the island and a plateau at 2/3 appears.

### B. Case 2

As we slightly decrease the compactness of the BS, the non-BH effects are further enhanced. For an intermediate compactness rotating BS (case 2), the Poincaré map,

<sup>3</sup>We refer to plunge for the orbits that exit the CZV (the separatrix). In the BH case, these orbits end up plunging into the horizon, while in BSs there might be cases in which plunging orbits escape to infinity.

shown in Fig. 6, displays a much more intricate structure around subdominant resonances. First, the radius of the star increases; therefore, orbits are allowed to exist in its interior, which is precluded for BHs, and should lead to more prominent effects. Intriguingly, due to the aforementioned phenomenon, here we find for the first time degenerate resonant islands—namely, islands of stability occurring for two different ranges of the radial coordinate. In particular, Fig. 6 shows the typical exterior 2/3 island as well as two sets of Birkhoff chains for the 4/7 resonance: one in the exterior and one in the interior of the BS.

The rotation curve in Fig. 7 for  $\dot{r}(0) = 0$  (left panel) confirms all the above. Decreasing the compactness leads to a more prominent change in monotonicity when the secondary enters the star. This, in turn, allows for degenerate plateaus in both the interior and the exterior of the star's geodesics, with the interior plateau being wider than the exterior one. Again, choosing a different initial velocity, we can turn the inflection point of 2/3 resonance into a plateau, since the velocity pushes the orbit to traverse the island.



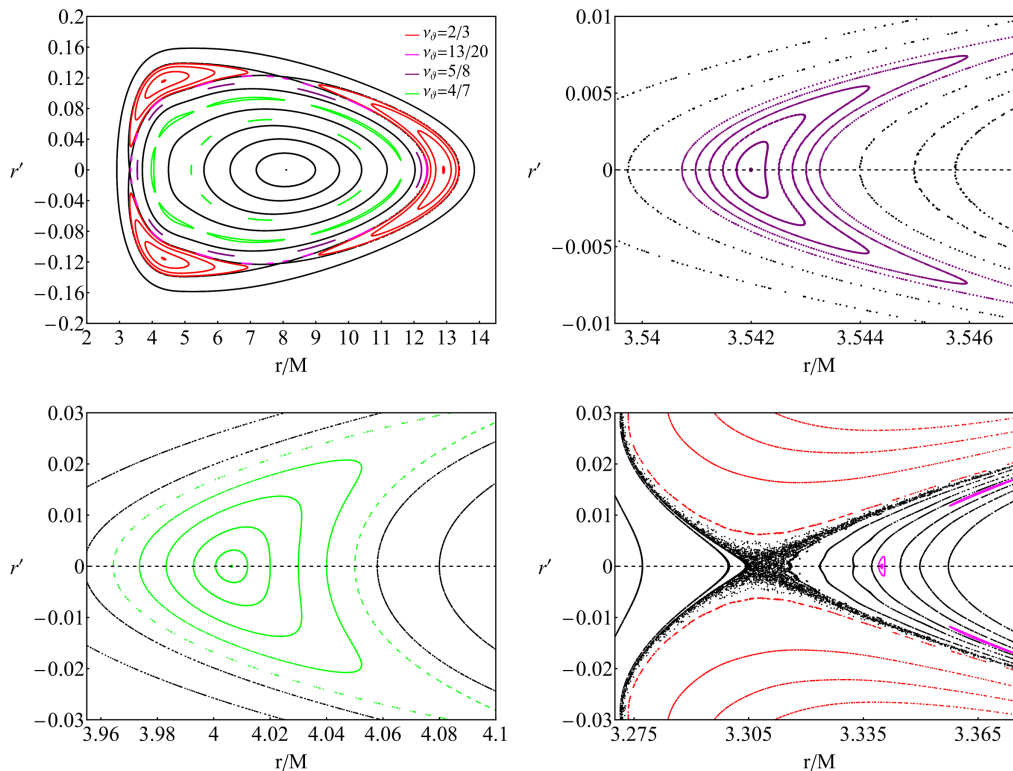


FIG. 8. Top left: the same as in Figs. 4 and 5 but for case 3 (smaller compactness,  $\mathcal{C} = 0.16$ ). Top right: enlargement of the region where the leftmost 5/8 island of stability resides. Bottom left: enlargement of the region where the leftmost 4/7 island of stability resides. Bottom right: enlargement of a region of the Poincaré map on the top left where a chaotic layer is present, shown with scattered black points that emanate from the unstable 2/3 periodic point with  $\dot{r}(0) = 0$ , and parts of two islands of stability, namely, the 2/3 and 13/20.

### C. Case 3

Case 3 is probably the most interesting one. Its relatively smaller compactness allows for a plethora of new phenomena in both Poincaré maps (Fig. 8) and rotation curves (Fig. 9). The radius of the BS increases even more, and the CZV enters deep inside the star where bound geodesics are still possible. This leads to a multitude of dominant and subdominant resonances, as shown in the top left panel in Fig. 8, as well as further degenerate Birkhoff chains. In the top right and bottom left panels, an enlargement of the interior 5/8 and 4/7 islands is presented. Probably the most interesting feature is displayed in the bottom right panel. Two islands of stability appear, namely, the 2/3 (in red) and the interior 13/20 part of the island (in pink). Furthermore, we find a visible chaotic layer that surrounds the 2/3 island, designated with scattered black points. Their source is the unstable periodic point at  $\dot{r}(0) = 0$  and  $r(0) \sim 3.31M$ . To the best of our knowledge, this is the first case in which a chaotic layer appears for a motivated model of compact object without any pathologies. This layer should give rise to significant effects on rotation curves and eventual EMRIs crossing through the particular 2/3 island when the fluxes will be taken into account [117–119].

Figure 9 shows the significantly modified rotation curves with respect to a typical non-Kerr BH (see, e.g., [105–109,111–114,119]). Degenerate 4/7 plateaus are visible in the interior and exterior of the star as well as a robust internal plateau for the 5/8 resonance. Although finding its external counterpart requires extreme fine-tuning, it is guaranteed that such region exists in the exterior. Closing in to the plunge (i.e., the inner boundary of the CZV), deep inside the star, a very large inflection point appears, which after enlarging (see Fig. 9, bottom left) reveals a thick chaotic layer with ill-defined rotation numbers. We also find a couple of extremely subdominant islands for the 13/20 (also shown in Fig. 8) and 15/23 resonances. Even more interestingly, by assuming an appropriate initial velocity for the geodesics, we managed to find, for the first time, an island (which leads to a plateau) that begins from the exterior of the star and ends in the interior. Its width ( $\sim 2.6M$  in quasi-isotropic or  $\sim 3.6M$  in Boyer-Lindquist coordinates) is so widespread that it supersedes any other plateau ever found in non-Kerr spacetimes, where the widest one found is of the order of  $\sim 0.05M$  (in Boyer-Lindquist coordinates) and barely compares with the plateaus for case 1 (2/3 resonance) and case 2 (4/7 resonance) island widths. Nevertheless, we

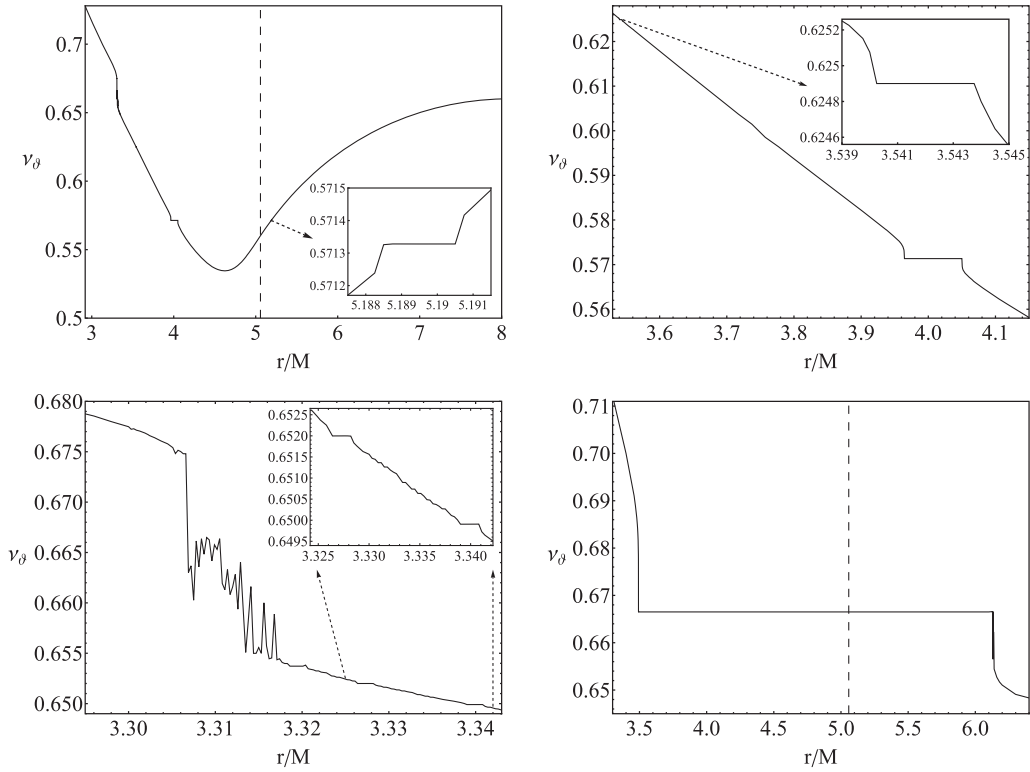


FIG. 9. Top left: rotation curve corresponding to the same system as in Fig. 8. The vertical dashed line represents the radius of the BS, while the inset enlarges the surrounding region of the external  $4/7$  plateau. Top right: enlarged part of the rotation curve on the top left figure on the subdominant resonances  $\nu_\theta = 5/8$  and  $4/7$  in descending order. Bottom left: enlarged part of the rotation curve on top left figure at the chaotic layer of the unstable periodic point for  $2/3$  resonance. A further enlargement is shown in the inset of two extremely subdominant islands with  $\nu_\theta = 15/23$  and  $13/20$  in descending order. Bottom right: rotation curve for the same parameters and initial conditions as in the top left figure but with  $\dot{r}(0) = 0.155$ . The initial velocity gives access to the  $2/3$  island of stability.

need to point out that the width of each island found in this and other similar studies are initial-condition dependent, according to their multiplicity. Therefore, maximizing their width is a tedious task. A better method would be to fix an initial condition, such as  $\dot{r}(0) = 0$ , and cross the islands forming beyond the central periodic point of the Poincaré map. In a geodesic analysis, this is perfectly doable in normal timescales and without accumulating significant error during the orbital evolution, though an inspiral trajectory close to the plunge is much faster to produce with minimized numerical error, in contrast to the islands on the right side of the central point where the fluxes are much smaller and the evolution time needs to be increased a lot, which, in turn, gives rise to larger errors.

For completeness, in Fig. 10, we present all rotation curves obtained with  $\dot{r}(0) = 0$  and varying  $r/M$ , together with the rotation curve of a Kerr BH with  $\chi = 0.8$ . The differences between BH orbits and noncompact rotating BSs are evident, and the BSs present novel features due to the absence of an event horizon. For fixed  $E$  and  $L_z$ , we find that even the most compact configuration considered differs dramatically from that of Kerr, while the rest completely disengage with the typical behavior of a Kerr rotation curve. Perhaps a rotation curve in the lines of those

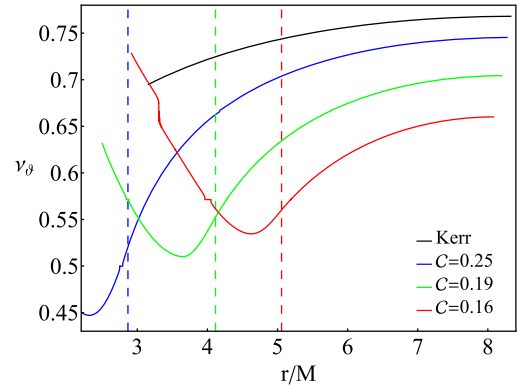


FIG. 10. Combined rotation curves of a secondary with  $m = 1M_\odot$  orbiting around a rotating BS with  $M = 10^6M_\odot$ , varying compactness  $\mathcal{C}$ , and  $\chi = 0.8$ . The secondary's conserved energy and angular momentum are  $E/m = 0.95$  and  $L_z/m = 3M$ , respectively. The fixed initial conditions chosen here are  $\dot{r}(0) = 0$  and  $\theta(0) = \pi/2$ , and  $\dot{\theta}(0)$  is defined by the constraint equation to guarantee bound motion, while  $r(0)$  is varied. The horizontal dashed lines represents the radii of each BS configuration. For comparison, we include the rotation curve of a Kerr BH with the same spacetime and geodesic parameters.

presented in [106,112] may seem more similar to that of case 1 BS but still the existence of the radius, the change in monotonicity when the orbits enters the star, the degenerate plateaus, and the existence of an observable chaotic layer should make rotating BSs have a contrasting and discernible behavior of geodesics when compared to those of non-Kerr spacetimes.

## V. ADIABATIC INSPIRAL AND WAVEFORMS

Inspirals in the EMRI limit can be conveniently described within BH perturbation theory [167,175]. Owing to the hierarchy of scales, the dynamics can be studied as a small perturbation of the geodesic motion of the secondary test mass around the primary object. To leading order in the mass ratio, one could evolve geodesic quantities adiabatically by taking into account dissipation due to radiative degrees of freedom. Higher-order corrections require including conservative and, in general, self-force effects during the inspiral [167,175–178].

While this program has been extremely successful for standard EMRIs around a Kerr BH within general relativity, going beyond the standard paradigm is much more challenging, even at the leading order. Indeed, dissipative corrections are computed using the Teukolsky formalism [179–181], which allows separating the perturbations of a Kerr BH in general relativity and computing fluxes through numerical integration of inhomogeneous ordinary differential equations with a point-particle source term [182,183]. This technology has been widely tested in the frequency [184–186] and time domain [187–190]. However, it heavily relies on the separability of the perturbation equations, which does not occur if the background is not described by the Kerr metric as in our case (which is, in addition, known only numerically). Likewise, the gravitational self-force was computed up to second order in perturbations [175,191,192] for orbits around BHs [177,193], but the case of ECOs is an uncharted territory.

In the absence of a consistent framework to study EMRI dynamics around a non-Kerr spinning object, here we use the only framework available at the moment, namely, approximate semirelativistic inspirals [194,195] and waveforms with methods known as “kludge” schemes [196–198]. Kludge waveforms are constructed through the so-called numerical kludge scheme, namely, by combining flat spacetime weak-field (PN) GW emission together with a fully relativistic treatment for the secondary’s motion.

### A. Numerical kludge scheme

To approximate EMRIs around rotating BSs, we integrate the second-order dynamical system for  $r, \theta$ , augmented with weak-field PN fluxes for the energy and angular momentum loss due to GW emission [194,195,199]. This treatment, though approximate and valid only for small orbital velocities, takes into account the dominant contribution of the

secondary’s radiative backreaction to the primary’s geometry, at second PN order, and results in an adiabatic evolution of the EMRI. During the evolution, the orbit is treated, at small timescales, as a geodesic, while for longer timescales the trajectory is slowly driven through consecutively damped geodesics. This scheme has been shown to perform well when compared to Teukolsky-based waveforms of EMRIs [198].

BSs have nontrivial multipolar structure which differs from the one of a Kerr BH [44,45,101–104]. At second PN order, the kludge scheme [194] involves the mass quadrupole moment  $M_2$ . Thus, to construct a more faithful (though still approximate) inspiral around a rotating BS, we augment the fluxes with its modified mass quadrupole moment (see [105,106,117,118,200,201]). This kludge scheme, together with the modified mass quadrupole moment, has recently been examined and found to provide results qualitatively equivalent to evolutions with instantaneous self-force in non-Kerr electromagnetic analogs, which indicates that this method can, in principle, describe resonance and island crossings in nonintegrable EMRIs with sufficient accuracy [202].

We employ linear variations of  $E$  and  $L_z$  in an iterative way, such that [117,118,203]

$$E_1 = \frac{E(0)}{m} + \left\langle \frac{dE}{dt} \right\rangle_{t=0} N_r T_r, \quad (14)$$

$$L_{z,1} = \frac{L_z(0)}{m} + \left\langle \frac{dL_z}{dt} \right\rangle_{t=0} N_r T_r, \quad (15)$$

where  $E(0)$  and  $L_z(0)$  are the energy and  $z$  component of the angular momentum at  $t = 0$ , respectively. In turn,  $\langle dE/dt \rangle_{t=0}$  and  $\langle dL_z/dt \rangle_{t=0}$  are the averaged PN fluxes calculated at the beginning of the inspiral, through the complicated equations outlined in [118,195].  $N_r$  is the number of radial periods elapsed between each update of (14) and (15), which improves the scheme and includes cumulative nonlinear variations, while  $T_r$  is the radial period of the EMRI. Equations (14) and (15) are iterated along the whole EMRI evolution with appropriate choices of  $N_r$  and  $T_r$  to obtain the dissipative orbit. If the system was integrable, then, through the evolution of the Carter constant, we would be able to also evolve the rest of the components of the angular momentum, namely,  $L_x$  and  $L_y$ , which are imprinted in Carter’s constant. Our case, though, is nonintegrable and lacks a separation Carter-like constant; therefore, we have no explicit way of evolving  $L_x$  and  $L_y$ , but rather we keep them constant.

Even though, due to dissipation, the constraint equation (5) is not anymore a constant of motion (that can be monitored to assess the accuracy of the numerical scheme), we have tested numerous random time instants of the inspirals obtained with the aforementioned scheme from which we extract the instantaneous position and velocity

vectors of the orbit,  $E$  and  $L_z$ , and calculate (5) for these values. We then compare the resulting constraint with the one obtained by evolving a geodesic with the aforementioned parameters of the same time instants as initial conditions. For all cases, we find that the new dissipated constraint is satisfied to within one part in  $10^7$  for the first  $\sim 10^4$  revolutions. Through geodesic evolutions of successive time instants of an inspiral, we can build dissipative Poincaré maps with adiabatically decreasing  $E$  and  $L_z$  and, therefore, calculate time-dependent rotation curves [111,118].

### B. GW modeling

To present the phenomenological imprints of inspiraling secondaries onto supermassive BSs, we employ the quadrupole approximation. In the traceless and transverse gauge, the metric perturbations read (e.g., [131])

$$h_{ij} = \frac{2}{d} \frac{d^2 Q_{ij}}{dt^2}, \quad (16)$$

where  $Q_{ij}$  is the symmetric and trace-free (STF) mass quadrupole tensor, which can be written as

$$Q^{ij} = \left[ \int x^i x^j T^{tt}(t, x^k) d^3x \right]^{\text{STF}}, \quad (17)$$

with  $t$  the coordinate time of the secondary source and

$$T^{tt}(t, x^i) = m \delta^{(3)}[x^i - Z^i(t)]. \quad (18)$$

Here, we employ the approximation where quasi-isotropic coordinates at infinity are identified with spherical ones as  $Z(t) = (x(t), y(t), z(t))$ , where

$$x(t) = r(t) \sin \theta(t) \cos \phi(t), \quad (19)$$

$$y(t) = r(t) \sin \theta(t) \sin \phi(t), \quad (20)$$

$$z(t) = r(t) \cos \theta(t), \quad (21)$$

and then transform them from spherical to Euclidean coordinates that describe the secondary's trajectory.

An incoming wave from an EMRI onto an interferometer can be projected in two polarizations,  $+$  and  $\times$ , by introducing two unit vectors  $\hat{p} = \hat{n} \times \hat{z} / |\hat{n} \times \hat{z}|$  and  $\hat{q} = \hat{p} \times \hat{n}$  (here,  $\times$  is the cross product of two vectors and should not be confused with the cross polarization symbol of the incoming GW), which are defined in terms of a third unit vector  $\hat{n}$  that points from the EMRI source to the detector. Finally, the unit vector  $\hat{z}$  designates the spin direction of the BS. The triplet  $\hat{p}, \hat{q}, \hat{n}$  forms an orthonormal basis from which the polarization tensor components are defined as

$$\epsilon_+^{ij} = p^i p^j - q^i q^j, \quad \epsilon_\times^{ij} = p^i q^j + p^j q^i \quad (22)$$

and allow us to write the metric perturbation in the quadrupole approximation as

$$h^{ij}(t) = \epsilon_+^{ij} h_+(t) + \epsilon_\times^{ij} h_\times(t), \quad (23)$$

where  $h_{+,\times}$  are the plus and cross polarizations, respectively, of the incoming GW. The GW components are then expressed in terms of the position  $Z^i(t)$ , velocity  $v^i(t) = dZ^i/dt$ , and acceleration  $a^i(t) = d^2Z^i/dt^2$  vectors. One finally obtains

$$h_{+,\times}(t) = \frac{2m}{d} \epsilon_{ij}^{+,\times} [a^i(t) Z^j(t) + v^i(t) v^j(t)]. \quad (24)$$

LISA's response to an incident GW event is correlated with the antenna pattern functions  $F_{I,II}^{+,\times}(t)$ , describing the motion of the detector on its respective spacecraft channels  $I$  and  $II$  (see Refs. [112,204,205] for details). The total waveform detected by a LISA-like interferometer reads

$$h_{I,II}(t) = \frac{\sqrt{3}}{2} [F_{I,II}^+(t) h_+(t) + F_{I,II}^\times(t) h_\times(t)]. \quad (25)$$

We assume a detector that lies at a luminosity distance  $d$  with fixed orientation  $\mathbf{n} = (0, 0, 1)$  with respect to the EMRI source and that the primary's polar and azimuthal angles are fixed at the equatorial plane. The data streams that will be considered in what follows will contain the GW together with stationary and Gaussian noise. For simplicity, we will further assume that the two data stream channels are uncorrelated; thus, we will abide to a single-channel approximation of our detector.

### VI. EMRIs AROUND A SPINNING BS

In this section, we discuss the effects of nonintegrability and chaos on EMRI evolution and GW emission. Even though approximate, the results shown below demonstrate the basic features of the chaotic phenomena taking place in rotating BSs. Since the most interesting cases of the BSs constructed are cases 1 and 3, we will focus on them from now on. We fix  $E(0)/m = 0.95$  and  $L_z(0)/m = 3M$  as initial parameters of the secondary in Eqs. (14) and (15), respectively, and perform a different numbers of updates depending on how quick the inspiral evolves, namely, how close we are to the inner boundary of the CZV (separatrix).

Note that in some cases the inspiral would occur *inside* the BS. This is a striking difference with respect to the BH case, in which the signal disappears after the particle has crossed the horizon. We can, therefore, continue the evolution as long as the orbits do not cross the separatrix, where the inspiral plunges.

It is worth noticing that the potential inside the BS is approximately constant (see Fig. 1) and not particularly



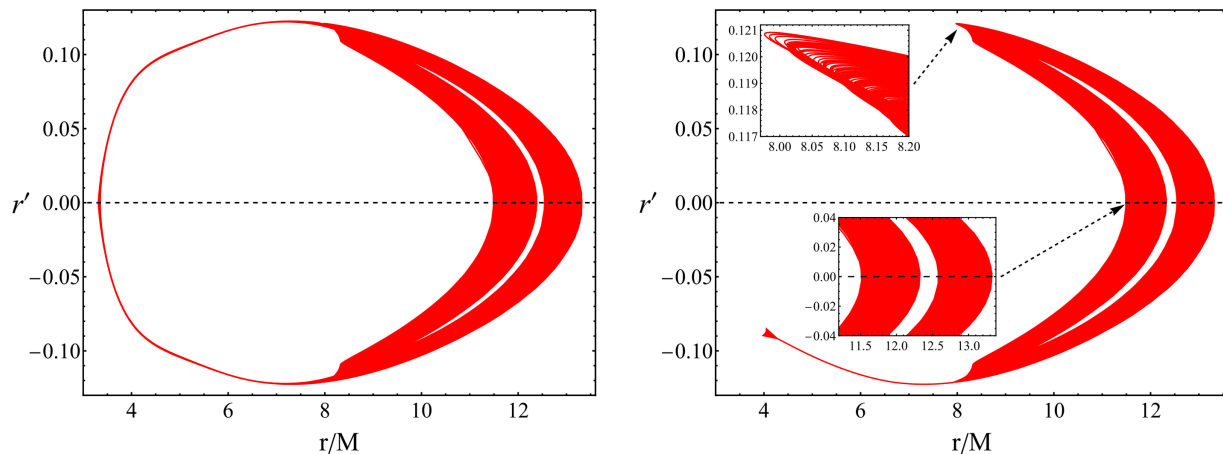


FIG. 11. Left: sustained resonance for case 3, with mass ratio  $m/M = 10^{-6}$ , and simplified linear fluxes without any updates as given in Eqs. (14) and (15). The secondary's initial parameters and conditions are  $E(0)/m = 0.95$ ,  $L_z(0)/m = 3M$ ,  $r(0) = 6.5M$ ,  $\dot{r}(0) = 0.155$ , and  $\theta(0) = \pi/2$ , while  $\dot{\theta}(0)$  is defined from the constraint equation (5). The total evolution time is  $t = 5 \times 10^6 M \sim 10$  months. The linearly dissipative inspiral spends roughly 1 month off resonance and 9 months in perfect resonance. Here, we have chosen a stroboscopic depiction for the trapping to be more easily identified; i.e., from the time series of the full Poincaré map, only every third consequent point is kept. Right: the same as in the left panel but starting from a point of the inspiral where the 1 month off resonance has lapsed and the orbit enters the (putatively) eternal resonance.

strong, which justifies the use of PN fluxes even inside the star. For EMRIs around Kerr, the overlap between PN and Teukolsky-based waveforms starts to completely deteriorate typically when the periastris radius  $r_p \sim 5M$  (in Boyer-Lindquist coordinates) or smaller [198], but in the BH case the potential is stronger, as shown in Fig. 1, due to the larger compactness at the horizon. Thus, our PN approximation should be accurate enough also inside the star all the way to the edge of the CZV, especially for the least compact configurations. Furthermore, we stress that we are only considering radiation-reaction effects, neglecting environmental effects such as dynamical friction and accretion within the BS [38] as well as direct (nongravitational) coupling between the secondary and the scalar field, both of which might significantly contribute to the inspiral.

### A. Sustained resonances

A first interesting result arises when we ignore the updates on the flux, Eqs. (14) and (15), an approximation that has been considered in various analyses [105,106,108]. This simplification leads to the following linearly varied fluxes:

$$E(t) = \frac{E(0)}{m} + \left\langle \frac{dE}{dt} \right\rangle \Big|_{t=0} t, \quad (26)$$

$$L_z(t) = \frac{L_z(0)}{m} + \left\langle \frac{dL_z}{dt} \right\rangle \Big|_{t=0} t. \quad (27)$$

Such assumption inevitably leads to sustained resonances that cannot exist in Kerr [206], where the secondary is trapped in a resonant island for an extremely long

(potentially infinite) time. In Fig. 11, we present one such case, where a 10 month inspiral spends 1 month evolving normally and 9 months in perfect resonance. It never eventually escapes the island, at least for the timescale over we have evolved the EMRI. In order to identify the trapping more easily, Fig. 11 presents a stroboscopic depiction; i.e., from the time series of the full dissipative Poincaré map, only every third consequent point is kept due to the multiplicity of the  $2/3$  resonance.

The initial position for a sustained resonance to occur is not fine-tuned, but rather a quite large region of initial conditions  $r(0) \in [6.46, 6.58]M$  exists (which corresponds to  $[7.47, 7.59]M$  in Boyer-Lindquist coordinates), when fixing the rest of the parameters as  $\dot{r}(0) = 0.155$  and  $\theta(0) = \pi/2$  and defining  $\dot{\theta}(0)$  through the constraint equation (5). Similar results have recently been found in [111] for linear variations of the fluxes like Eq. (26). Even if the range of initial conditions giving such sustained resonances is not negligible, in practice such sustained resonances are an artifact due the assumption of low-order energy and angular-momentum fluxes throughout the evolution. Namely, the linear approximation in energy and angular momentum is valid as long as the trajectory of the EMRI does not get too far from the initial geodesic, on which the orbital elements and fluxes have been initialized.

By taking into account updates (from 50 to 150 for some representative cases) on the fluxes for the aforementioned radial range, which effectively includes nonlinear terms on the fluxes, all sustained resonances vanish. Of course, we cannot exclude the possibility that the region of sustained resonances either shrinks significantly or hides into a different range of initial conditions, although we consider

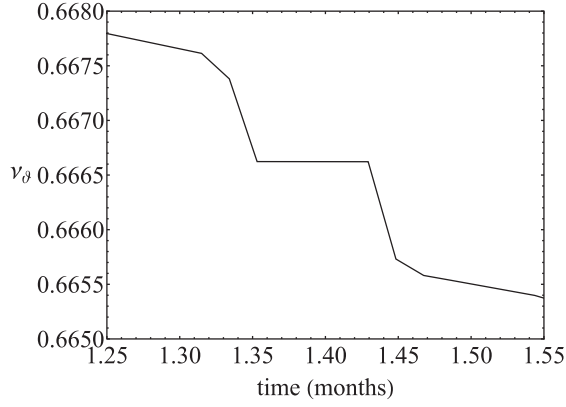


FIG. 12. External  $2/3$  resonant island crossing for case 1. To produce the inspiral, we have updated the fluxes 300 times. The secondary's initial parameters and conditions are  $E(0)/m = 0.95$ ,  $L_z(0)/m = 3M$ ,  $r(0) = 5.026M$ ,  $\dot{r}(0) = 0.1$ , and  $\theta(0) = \pi/2$ , while  $\dot{\theta}(0)$  is defined from the constraint equation (5). The EMRI spends  $\sim 200$  cycles in resonance.

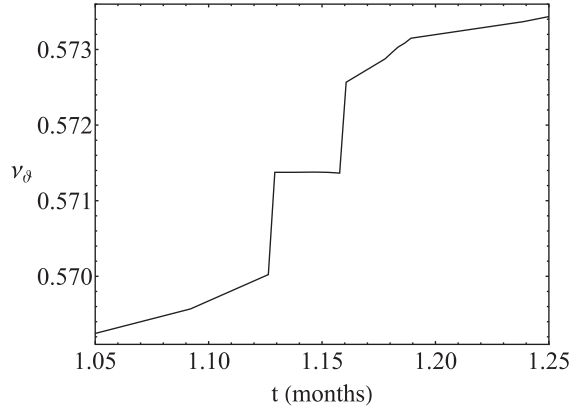


FIG. 13. Internal  $4/7$  resonant island crossing for case 3. To produce the inspiral, we have updated the fluxes 250 times. The secondary's initial parameters and conditions are  $E(0)/m = 0.95$ ,  $L_z(0)/m = 3M$ ,  $r(0) = 4.06025M$ , and  $\dot{r}(0) = 0$ ,  $\theta(0) = \pi/2$  while the  $\dot{\theta}(0)$  is defined from the constraint equation (5). The EMRI spends  $\sim 100$  cycles in resonance.

this option as unlikely. Note also that putative sustained resonances should persist (and not disappear) as the number of flux updates is increased. A similar case was recently studied for an EMRI analog in [202], where lower-order flux approximations gave rise to sustained resonances, whereas, when higher-order terms were involved, the sustained resonances disappeared.

### B. Time-dependent rotation curves

Figures 12 and 13 show typical, time-dependent, island crossings for cases 1 and 3. In Fig. 12, the nonzero initial velocity leads to the EMRI crossing the  $2/3$  island in the exterior of the case 1 configuration. The plateau is finite and lasts for around 200 revolutions before it exits the

island. The fact that the rotation number decreases with time shows that the orbital motion is outside of the star and tends toward circularization. On the other hand, in Fig. 13, we show the dissipative rotation curve of the  $4/7$  island crossing which resides inside the BS of case 3. The fluxes have increased at this point significantly; therefore, the EMRI evolves faster. Nevertheless, the secondary spends  $\sim 100$  cycles in perfect resonance which is extraordinary for a subdominant resonance. Equivalently, the fact that these orbits are inside the star and both the eccentricity and rotation numbers increase justifies why the dissipative rotation curve increases with time.<sup>4</sup>

The final and most interesting scenario examined for case 3 is the very large plateau that arises when  $\dot{r}(0) = 0.155$  that begins from the exterior and ends in the interior of the BS. Even though one would expect a dissipative rotation curve with a plateau that lasts for thousands of cycles, the existence of a thick chaotic layer around the island induces a significant alteration to the rotation curve, which we find here for the first time. In Fig. 14, we present the behavior of the wide  $2/3$  island. On the left, we show that, instead of a plateau, we encounter mostly the chaotic layer [regardless of the initial condition  $r(0)$ ], where the rotation numbers are ill defined. Nonetheless, there are points (marked in red in the enlarged inset in the left panel in Fig. 14) that actually enter the island. To make sure that these points do enter the resonance, we plot on the right the corresponding KAM curves of these points. As shown, they form islands with tips that do not touch; therefore, the EMRI is not occupying the chaotic layer, unlike the rest of the black points in the inset in Fig. 14 that correspond to orbits residing in the chaotic layer. What seems to occur here is a strong chaotic shielding which does not allow the EMRI to spend continuous time intervals inside the island. Even so, we should expect interesting GW imprints for all cases discussed above and especially those from case 3, which take place in the interior of the rotating BS. We present those effects in the next section.

We stress that our results are based on PN fluxes and neglect effects other than radiation reaction within the BS, e.g., dynamical friction and accretion, which can nevertheless be added into the evolution.

### C. GW frequency evolution

After obtaining the inspirals for cases 1 and 3, it is straightforward to use Eq. (25) in order to find the approximate GW emitted by such EMRIs. The time-domain waveforms are Fourier transformed to the

<sup>4</sup>It has been shown that, before plunge, Kerr EMRIs enter a short phase of increasing eccentricity [195]. In our case, due to the absence of an event horizon, the eccentric EMRI can enter the star and the eccentricity continues increasing and leads to orbits as those found in [94]. Since the eccentricity is directly proportional to the periastron-apoapsis oscillation frequency  $\omega_r$ , the rotation number increases as well.

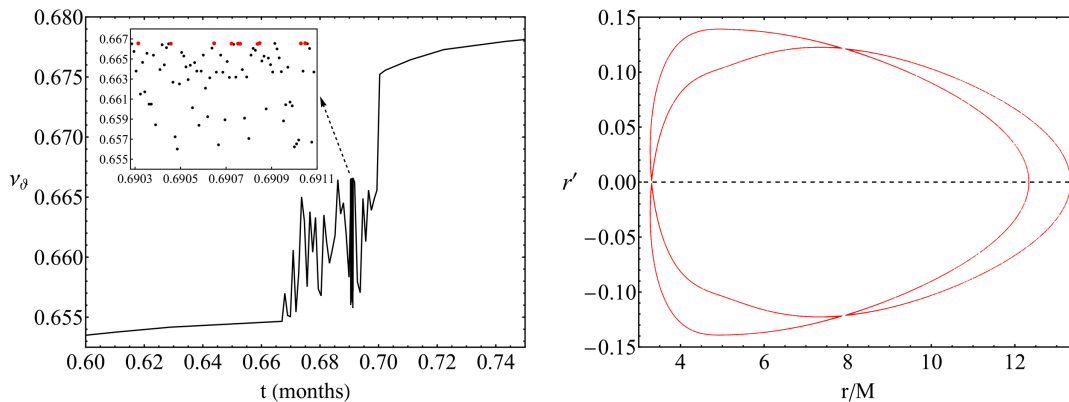


FIG. 14. Left: interior  $2/3$  resonant island crossing for case 3. To produce the inspiral, we have updated the fluxes 200 times. The secondary's initial parameters and conditions are  $E(0)/m = 0.95$ ,  $L_z(0)/m = 3M$ ,  $r(0) = 6.5M$ ,  $\dot{r}(0) = 0.155$ , and  $\theta(0) = \pi/2$ , while  $\dot{\theta}(0)$  is defined from the constraint equation (5). The EMRI spends  $\sim 10$  cycles on and off the resonant island and  $\sim 100$  revolutions in the vicinity of the  $2/3$  Birkhoff chain until the chaotic layer and island are crossed. Right: the produced KAM curves from the red dots shown in the inset in the left panel. All of them (namely, ten points) belong to the  $2/3$  resonant island.

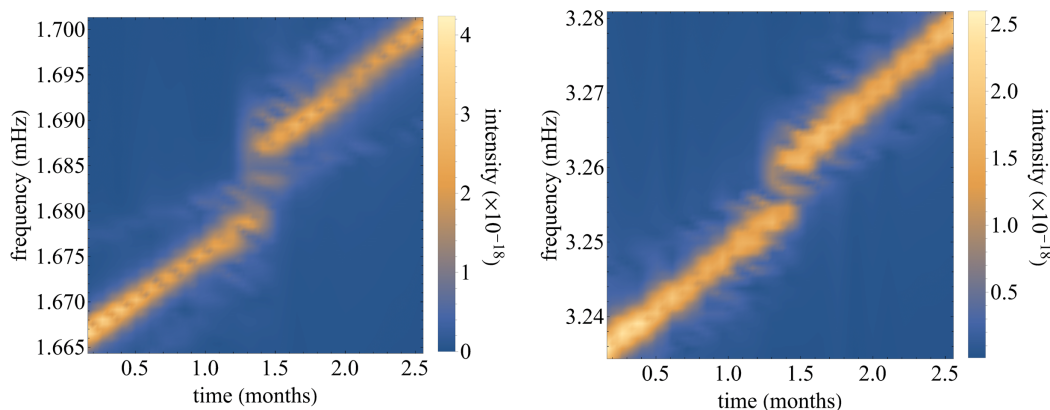


FIG. 15. Frequency evolution of an EMRI around rotating BS from case 1, through the  $2/3$  resonant island with parameters and initial conditions as in Fig. 12. As a reference, the approximate GWs (fundamental frequency in the left panel and first harmonic in the right panel) are detected at luminosity distance  $d = 100$  Mpc.

frequency domain where the frequency evolution of the inspiral can be constructed. Here, we follow [117–119] and construct the spectrograms by performing consecutive short-time Fourier transforms, with appropriate window sizes and offsets in order to maximize the quality of the resulting figures.

In Fig. 15, we present the most typical glitch waveform for case 1, where the BS is rather compact and mimics a non-Kerr BH. Its fundamental and first-harmonic frequency evolution display the standard modulation that occurs when the EMRI crosses the  $2/3$  island (that lies on the exterior of the rotating BS and lasts for 200 revolutions). This should lead to a significant dephasing with respect to an integrable EMRI evolution that crosses the same resonance. The resemblance with glitches found in [117,118] for non-Kerr spacetimes is remarkable. Therefore, since we use the hybrid kludge scheme and the quadrupole formula, in this case it would be almost impossible to distinguish between

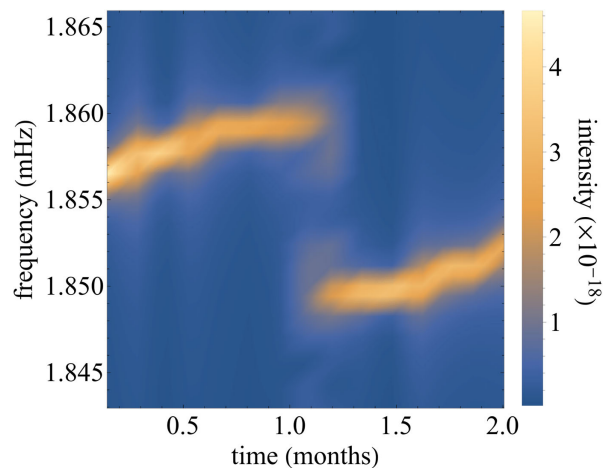


FIG. 16. The same as Fig. 15 but for the rotating BS configuration of case 3, through the  $4/7$  interior resonant island with parameters and initial conditions as in Fig. 13.

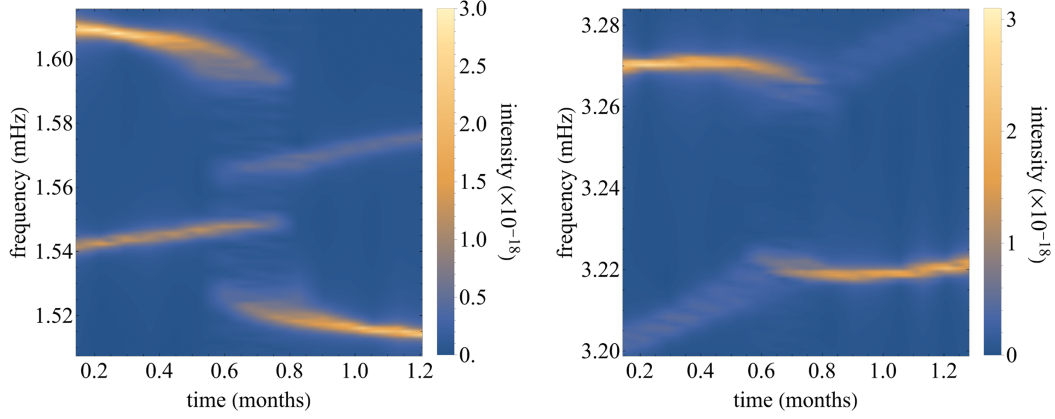


FIG. 17. The same as Fig. 15 but for the rotating BS configuration of case 3, through the  $2/3$  interior Birkhoff chain with parameters and initial conditions as in Fig. 14.

non-Kerr BHs or rotating BS based only on these glitches. Fortunately, case 3, the less compact configuration we have constructed, changes this picture completely. Figure 16 shows the frequency evolution of an EMRI through the internal  $4/7$  island. The frequency evolution becomes nonlinear due to the acceleration of the fluxes and the EMRI frequencies after the glitch increase toward a chirp.

Finally, we examine the spectrogram of an EMRI crossing the internal  $2/3$  resonant island that corresponds to the inspiral shown in Fig. 14. The GW frequency modulation shown in Fig. 17 is the first one of its kind found in any nonintegrable spacetime so far. We observe not only similar nonlinear frequency evolution as a function of time for the strongest Fourier peaks (fundamental and first harmonic) as in Fig. 16, but also linear-in-time subdominant frequency peaks that evolve and glitch in a similar manner. We have performed the same inspiral for two different initial conditions  $r(0)$ —one that lies outside and one that lies inside the range of sustained resonances (if linear fluxes are assumed)—and the resulting spectrogram is qualitatively the same as that shown in Fig. 17. This feature is significantly different from all the other glitches found in previous nonintegrable spacetimes and is associated to the fact that the plateau in the dissipative rotation curve is replaced with an observable chaotic layer with glimpses of island occupancy.

When an orbit is fully chaotic and resides in a chaotic sea [133], then we expect rotation curves and spectrograms to be rendered useless, since no well-defined rotation numbers and discrete GW frequencies exist [201,207]. On the other hand, when an orbit is close to a slightly chaotic region but otherwise not a fully chaotic part of phase space, such as the chaotic layer that shields the interior  $2/3$  island of case 3, the waveform and its frequency content resemble a lot those of a regular orbit, with discrete Fourier peaks and indistinguishable effects of chaos in the time-domain waveform. The only key difference is that the discrete Fourier peaks are not comprised by single harmonics (for geodesics) but rather harmonics that are broken down to

subpeaks. The spectrum, nevertheless, remains discrete. This has been shown in [207] for a secondary particle with spin orbiting around a Schwarzschild BH (see Figs. 4, 10, 11, and 13 therein), although in that case this behavior disappears as the secondary spin is treated perturbatively, as also requested for consistency within the perturbative expansion in the mass ratio (see, e.g., [208]). It is, therefore, interesting that we recover the same feature, that is a slightly chaotic region that embeds the island, but otherwise normal generic orbits around this region, discrete Fourier spectra, and harmonics with multiple peaks but in rotating BS spacetimes (where motion is not even integrable in a perturbative sense). This is the reason why Fig. 17 has such a distinctive and peculiar nature, which can be explained by the effects discussed in [207]. If we consider the effects on the spectrogram and the dissipative evolution through the Birkhoff chain, the EMRI spends around 100 cycles to cross it and ten cycles in perfect resonance. Yet, a Birkhoff chain is composed of both stable and unstable periodic points, and the chaotic layer helps to amplify the frequency glitch in a significant way, with frequency jumps as large as  $\sim 0.07$  mHz for the most dominant fundamental Fourier peak evolution, which is almost one order of magnitude larger than any other frequency glitches presented here and also higher than those found in [117,118] for various deformation parameters that were either exaggerated or chosen arbitrarily. Our case presents a well-motivated model of ECOs that has a precise formation scenario; thus, the results presented here can be used in the future as a test bed to understand if weak or strong (or no) chaos exists in GW observations.

## VII. CONCLUSIONS

The detection of EMRIs by LISA [121] and other spaceborne detectors [126–128] will provide for the first time an extremely accurate mapping of the primary’s spacetime geometry, due to the large mass hierarchy that creates the conditions for long-lasting inspirals with continuously



observable GW emission. The associated signal will present very rich phenomenology [123] like the appearance of resonances [105,107,108,111] and, remarkably, carries information about spacetime symmetries [106,112].

The observation of these systems will also help to decide if BHs are the only compact objects in the Universe or if other exotic configurations exist in nature. The different multipolar structure, relative to Kerr BHs, can lead to fascinating phenomena around resonances such as frequency modulation and GW glitches [117], in particular, for those spacetimes that lack a Carter constant (or any other higher-rank Killing tensor) that would guarantee the integrability of geodesics. So far, only bumpy and non-Kerr solution of general relativity—that are plagued with pathologies [118,119] and do not come from a well-motivated, first-principle theory—have been analyzed in order to inspect their different phenomenology.

Here, we considered for the first time one of the most well-behaved and simple compact object that may as well exist in our Universe, namely, rotating BSs. These exotic objects, which lack an event horizon or singularities, have a clear formation mechanism and can serve as prototypical BH mimickers. They also constitute compelling dark matter candidates and could have formed in the early Universe, e.g., as remnants of inflation.

While the majority of analyses for BSs have been performed for equatorial orbits, here we took a different turn on examining supermassive self-interacting rotating BSs in the context of EMRIs for generic orbits (without constraints on the orbital plane or eccentricity). In an attempt to study geodesics that are peculiar enough to be distinguishable from those around Kerr BHs, we evolved geodesics around and inside supermassive rotating configurations and studied their GW signatures. We have built numerically three such configurations with representative values of the spin and compactness.

Our geodesic analysis reveals the existence of resonant islands (with finite width) and Birkhoff chains in the phase space of orbits, which signals that rotating BSs are non-integrable. We also found that compact rotating BSs behave similarly to non-Kerr BHs up to the point where the geodesic enters the star smoothly and the geodesic structure becomes qualitatively different. Decreasing the compactness makes things much more different between rotating BSs and non-Kerr BHs. First, the geodesic phase space hosts many orbits that reside in the star's interior, where the rotation curve exhibits a change in monotonicity and begins to increase due to the increment of eccentricity [94]. The latter effect leads to a newly found phenomenon, that is, the existence of degenerate islands of stability, in the interior and the exterior of the star, with the same rotation number. We have also found regions in the phase space of geodesics where there exist not only a plethora of resonant islands, but also a thin chaotic layer surrounding

the most dominant  $2/3$  island of stability. This is, to our knowledge, the first time that a full Birkhoff chain appears in a general relativistic setup, which has important implications in GWs emitted by EMRIs that cross this region. With appropriate initial conditions, we find that the  $2/3$  island encounters a plateau in the rotation curve, where the geodesic enters the island in the exterior and exits in the interior of the star, a fascinating outcome of the fact that the compactness of the BS of case 3 (albeit as large as a typical neutron star) is relatively smaller than in the other cases.

To achieve some initial estimates of the elementary structure of approximate waveforms from such rotating BSs, and especially for generic inspirals that cross transient resonances, we use the quadrupole approximation to model GWs and evolve the inspiral, with augmented PN fluxes to account for the modified multipolar structure of our configurations [45,104]. Despite these approximations, the phenomenology of the inspiral and GW signal is expected to be robust.

At first sight with a linear approximation of the fluxes, we stumble upon inspirals that enter the  $2/3$  island, in a generous range of initial conditions  $r(0)$ , and never exit the resonance, as also found in [111] but in a much smaller radial domain. However, when we consistently update fluxes during the inspiral (though in a discretized way after some number of revolutions), higher-order terms seem to destroy such sustained resonances. Although unlikely, we cannot unequivocally exclude the existence of other regions of phase space where such resonances occur even when updates in the fluxes are introduced. We sketch the dissipative rotation curves by using time instants of each EMRI as initial condition to a geodesic evolution and find that external resonant islands are indistinguishable with those occurring in non-Kerr objects [117–119]. The plateaus that characterize islands situated in the interior of the star are approached from below in the rotation curves, which then reprise a monotonically increasing behavior. This corresponds to a reversed time and radial dependence with respect to the rotation curves in the neighborhood of external islands, related to the nonzero energy-density distribution inside the star. Such monotonicity reversal also pairs with the different evolution of the eccentricity. Indeed, inside the star, eventually a point is reached where the circularization of orbits has lapsed and the eccentricity increases with decreasing radius, in contrast to what happens in the exterior. The most prominent island of all found to date, the one for case 3 that has a record width of  $2.6M$  (in quasi-isotropic coordinates), is even more complicated due to chaotic shielding. The EMRI does not enter and stay in the island but rather oscillates between on and off island states. It manages to do so at least ten times during which the evolution drives the orbit around the chaotic layer till the secondary eventually exits the particular part of the Birkhoff chain.

Overall, the time spent in these cases spans from 200 cycles in external resonances, where the evolution is adiabatically slow, to around 100 cycles in the interior of the star, when the Birkhoff chain is taken into account as a part of the whole chaotic KAM curve (and not just the island with the periodic stable point at its center).

When the EMRI crosses a resonant island, all the above effects are imprinted onto the EMRI waveform either in a typical way, analogous to other non-Kerr systems, or as novel signatures that designate the existence of a supermassive BS primary. GW signals from the exterior islands are qualitatively indistinguishable from those in non-Kerr EMRIs, a result which is expected from the close similarity in the rotation curves discussed above. The case of internal motion is, instead, quite different. Even subdominant resonant islands introduce significant nonlinear frequency modulation, because the orbits are close to exiting the CZV (see, e.g., Fig. 16). The widest resonant island of case 3 has a very special behavior imprinted in the GW when the EMRI crosses it. The proximity of the orbits to the otherwise mild (but still observable) chaotic layer leads to an effect in the GW Fourier peaks first found in [207]. Moderate chaotic layers do not produce continuous GW spectra, as fully chaotic orbits do, but rather discrete sets of harmonics that are broken down to subharmonics. This phenomenon is evident in Fig. 17, where two simultaneous glitches occur under to the evolution of each subfrequency due to mild chaos. The underlying reason is, again, the fact that the EMRI is close to crossing a thin chaotic region. This turns each single harmonic of the frequency content of the approximated GW signal into multiple subpeaks that arise in the spectrogram in the particular fashion shown in Fig. 17. The most prominent (the brightest) one, which leads to a frequency glitch of  $\mathcal{O}(0.1)$  mHz, renders all exterior glitches subdominant and should affect significantly the orbital evolution and eventual parameter estimation. Yet, we stress that our results are qualitative and should be extended with more accurate inspiral and waveform modeling.

In this respect, it would be very interesting to perform proper perturbation theory around a spinning BS, although

nonseparability of the equations makes the flux computation quite challenging compared to the Teukolsky case for a Kerr BH. Nevertheless, our results provide solid evidence that chaos does exist in EMRIs around rotating BSs, and the fact that this is a quite compelling model for ECOs should drive us to further understand these objects as well as their effects in geodesics and EMRI dynamics.

Along these lines, it would be relevant to include environmental effects such as dynamical friction and accretion [38,136–138] and assess their impact on the chaotic motion and EMRI signal. Finally, although we focused on a specific model of BS with large quartic interactions, we expect to find the same qualitative features in other spinning BS models, spinning Proca stars, and, in fact, all spinning ECOs where geodesic motion is most likely nonintegrable. In particular, we expect the same (and perhaps even more prominent) signatures of chaotic motion for EMRIs in generic orbits around BH microstates predicted in the fuzzball scenario (see [209] for a recent review), due to their rich multipolar structure and breaking of the axial and equatorial symmetry [210–214].

## ACKNOWLEDGMENTS

The authors are indebted to Georgios Lukes-Gerakopoulos and Kostas D. Kokkotas for insightful discussions. We acknowledge financial support provided under the European Union’s H2020 European Research Council (ERC), Starting Grant Agreement No. DarkGRA–757480 and support under the Ministero dell’Università e della Ricerca - Progetti di rilevante interesse nazionale (MIUR–PRIN) (Grant No. 2020KR4KN2 “String Theory as a bridge between Gauge Theories and Quantum Gravity”) and Framework per l’Attrazione e il Rafforzamento delle Eccellenze per la ricerca in Italia (FARE) (GW-NEXT, CUP: B84I20000100001, 2020KR4KN2) programs. K.D. is supported by the Deutscher Akademischer Austauschdienst (DAAD) program for the “promotion of the exchange and scientific cooperation between Greece and Germany IKYDAAD 2022” (57628320).

- 
- [1] R. Abbott *et al.* (LIGO Scientific and Virgo Collaborations), GWTC-2: Compact binary coalescences observed by LIGO and Virgo during the first half of the third observing run, *Phys. Rev. X* **11**, 021053 (2021).
  - [2] R. Abbott *et al.* (LIGO Scientific, KAGRA, and VIRGO Collaborations), Observation of gravitational waves from two neutron star–black hole coalescences, *Astrophys. J. Lett.* **915**, L5 (2021).
  - [3] R. Abbott *et al.* (LIGO Scientific, VIRGO, and KAGRA Collaborations), GWTC-3: Compact binary coalescences

- observed by LIGO and Virgo during the second part of the third observing run, [arXiv:2111.03606](https://arxiv.org/abs/2111.03606) [Phys. Rev. X (to be published)].
- [4] R. Abbott *et al.* (LIGO Scientific and Virgo Collaborations), GW190814: Gravitational waves from the coalescence of a 23 solar mass black hole with a 2.6 solar mass compact object, *Astrophys. J. Lett.* **896**, L44 (2020).
- [5] R. Abbott *et al.* (LIGO Scientific and Virgo Collaborations), GW190521: A binary black hole merger with a total mass of  $150M_{\odot}$ , *Phys. Rev. Lett.* **125**, 101102 (2020).

- [6] R. Abbott *et al.* (LIGO Scientific and Virgo Collaborations), Properties and astrophysical implications of the  $150M_{\odot}$  binary black hole merger GW190521, *Astrophys. J. Lett.* **900**, L13 (2020).
- [7] J. Calderón Bustillo, N. Sanchis-Gual, A. Torres-Forné, J. A. Font, A. Vajpeyi, R. Smith, C. Herdeiro, E. Radu, and S. H. W. Leong, GW190521 as a merger of Proca stars: A potential new vector boson of  $8.7 \times 10^{-13}$  eV, *Phys. Rev. Lett.* **126**, 081101 (2021).
- [8] V. Cardoso and P. Pani, Testing the nature of dark compact objects: A status report, *Living Rev. Relativity* **22**, 4 (2019).
- [9] E. Maggio, P. Pani, and G. Raposo, Testing the nature of dark compact objects with gravitational waves, in *Handbook of Gravitational Wave Astronomy*, edited by C. Bambi, S. Katsanevas, and K. D. Kokkotas (Springer, Singapore, 2021), 10.1007/978-981-15-4702-7\_29-1.
- [10] G. Bertone, D. Hooper, and J. Silk, Particle dark matter: Evidence, candidates and constraints, *Phys. Rep.* **405**, 279 (2005).
- [11] D. Clowe, M. Bradac, A. H. Gonzalez, M. Markevitch, S. W. Randall, C. Jones, and D. Zaritsky, A direct empirical proof of the existence of dark matter, *Astrophys. J. Lett.* **648**, L109 (2006).
- [12] L. Bergstrom, Dark matter candidates, *New J. Phys.* **11**, 105006 (2009).
- [13] J. R. Primack, Dark matter and structure formation, in *Proceedings of the Midrasha Mathematicae in Jerusalem: Winter School in Dynamical Systems* (Cambridge University Press, Cambridge, 1997), arXiv:astro-ph/9707285.
- [14] E. Corbelli and P. Salucci, The extended rotation curve and the dark matter halo of M33, *Mon. Not. R. Astron. Soc.* **311**, 441 (2000).
- [15] E. W. Kolb and M. S. Turner, *The Early Universe* (CRC Press, Boca Raton, 1990), Vol. 69.
- [16] S. M. Carroll, The cosmological constant, *Living Rev. Relativity* **4**, 1 (2001).
- [17] A. Del Popolo, Dark matter and structure formation a review, *Astronomy Reports* **51**, 169 (2007).
- [18] A. Arbey and F. Mahmoudi, Dark matter and the early Universe: A review, *Prog. Part. Nucl. Phys.* **119**, 103865 (2021).
- [19] L. Perivolaropoulos and F. Skara, Challenges for  $\Lambda$ CDM: An update, *New Astron. Rev.* **95**, 101659 (2022).
- [20] E. Seidel and W.-M. Suen, Formation of solitonic stars through gravitational cooling, *Phys. Rev. Lett.* **72**, 2516 (1994).
- [21] N. Sanchis-Gual, F. Di Giovanni, M. Zilhão, C. Herdeiro, P. Cerdá-Durán, J. A. Font, and E. Radu, Nonlinear dynamics of spinning bosonic stars: Formation and stability, *Phys. Rev. Lett.* **123**, 221101 (2019).
- [22] S. Bonazzola and F. Pacini, Equilibrium of a large assembly of particles in general relativity, *Phys. Rev.* **148**, 1269 (1966).
- [23] D. A. Feinblum and W. A. McKinley, Stable states of a scalar particle in its own gravitational field, *Phys. Rev.* **168**, 1445 (1968).
- [24] D. J. Kaup, Klein-Gordon geon, *Phys. Rev.* **172**, 1331 (1968).
- [25] R. Ruffini and S. Bonazzola, Systems of self-gravitating particles in general relativity and the concept of an equation of state, *Phys. Rev.* **187**, 1767 (1969).
- [26] M. Colpi, S. L. Shapiro, and I. Wasserman, Boson stars: Gravitational equilibria of self-interacting scalar fields, *Phys. Rev. Lett.* **57**, 2485 (1986).
- [27] J. J. van der Bij and M. Gleiser, Stars of bosons with nonminimal energy momentum tensor, *Phys. Lett. B* **194**, 482 (1987).
- [28] J. A. Frieman, G. B. Gelmini, M. Gleiser, and E. W. Kolb, Solitogenesis: Primordial origin of nontopological solitons, *Phys. Rev. Lett.* **60**, 2101 (1988).
- [29] J. A. Frieman, A. V. Olinto, M. Gleiser, and C. Alcock, Cosmic evolution of nontopological solitons. I, *Phys. Rev. D* **40**, 3241 (1989).
- [30] R. Ferrell and M. Gleiser, Gravitational atoms. 1. Gravitational radiation from excited boson stars, *Phys. Rev. D* **40**, 2524 (1989).
- [31] D. Grasso, Boson-star formation by classical instability, *Phys. Rev. D* **41**, 2998 (1990).
- [32] I. I. Tkachev, On the possibility of Bose star formation, *Phys. Lett. B* **261**, 289 (1991).
- [33] A. R. Liddle and M. S. Madsen, The structure and formation of boson stars, *Int. J. Mod. Phys. D* **01**, 101 (1992).
- [34] P. Jetzer, Boson stars, *Phys. Rep.* **220**, 163 (1992).
- [35] F. E. Schunck and E. W. Mielke, General relativistic boson stars, *Classical Quantum Gravity* **20**, R301 (2003).
- [36] S. L. Liebling and C. Palenzuela, Dynamical boson stars, *Living Rev. Relativity* **26**, 1 (2023).
- [37] M. Kesden, J. Gair, and M. Kamionkowski, Gravitational-wave signature of an inspiral into a supermassive horizonless object, *Phys. Rev. D* **71**, 044015 (2005).
- [38] C. F. B. Macedo, P. Pani, V. Cardoso, and L. C. B. Crispino, Astrophysical signatures of boson stars: Quasinormal modes and inspiral resonances, *Phys. Rev. D* **88**, 064046 (2013).
- [39] C. F. B. Macedo, P. Pani, V. Cardoso, and L. C. B. Crispino, Into the lair: Gravitational-wave signatures of dark matter, *Astrophys. J.* **774**, 48 (2013).
- [40] C. F. B. Macedo, V. Cardoso, L. C. B. Crispino, and P. Pani, Quasinormal modes of relativistic stars and interacting fields, *Phys. Rev. D* **93**, 064053 (2016).
- [41] V. Cardoso, E. Franzin, A. Maselli, P. Pani, and G. Raposo, Testing strong-field gravity with tidal Love numbers, *Phys. Rev. D* **95**, 084014 (2017); **95**, 089901(A) (2017).
- [42] H.-K. Guo, K. Sinha, and C. Sun, Probing boson stars with extreme mass ratio inspirals, *J. Cosmol. Astropart. Phys.* **09** (2019) 032.
- [43] E. Berti and V. Cardoso, Supermassive black holes or boson stars? Hair counting with gravitational wave detectors, *Int. J. Mod. Phys. D* **15**, 2209 (2006).
- [44] C. Pacilio, M. Vaglio, A. Maselli, and P. Pani, Gravitational-wave detectors as particle-physics laboratories: Constraining scalar interactions with a coherent inspiral model of boson-star binaries, *Phys. Rev. D* **102**, 083002 (2020).
- [45] M. Vaglio, C. Pacilio, A. Maselli, and P. Pani, Bayesian parameter estimation on boson-star binary signals with a



- coherent inspiral template and spin-dependent quadrupolar corrections, *Phys. Rev. D* **108**, 023021 (2023).
- [46] E. Seidel and W. M. Suen, Oscillating soliton stars, *Phys. Rev. Lett.* **66**, 1659 (1991).
- [47] S. R. Coleman, Q-balls, *Nucl. Phys.* **B262**, 263 (1985); **B269**, 744(A) (1986).
- [48] A. Kusenko and M. E. Shaposhnikov, Supersymmetric Q balls as dark matter, *Phys. Lett. B* **418**, 46 (1998).
- [49] K. D. Lozanov and M. A. Amin, Gravitational perturbations from oscillons and transients after inflation, *Phys. Rev. D* **99**, 123504 (2019).
- [50] J. C. Aurrekoetxea, K. Clough, and F. Muia, Oscillon formation during inflationary preheating with general relativity, *Phys. Rev. D* **108**, 023501 (2023).
- [51] K. D. Lozanov, M. Sasaki, and V. Takhistov, Universal gravitational wave signatures of cosmological solitons, [arXiv:2304.06709](https://arxiv.org/abs/2304.06709).
- [52] G. Franciolini and P. Pani, Stochastic gravitational-wave background at 3G detectors as a smoking gun for microscopic dark matter relics, [arXiv:2304.13576](https://arxiv.org/abs/2304.13576).
- [53] M. Gleiser, Stability of boson stars, *Phys. Rev. D* **38**, 2376 (1988); **39**, 1257(E) (1989).
- [54] M. Gleiser and R. Watkins, Gravitational stability of scalar matter, *Nucl. Phys.* **B319**, 733 (1989).
- [55] F. V. Kusmartsev, E. W. Mielke, and F. E. Schunck, Gravitational stability of boson stars, *Phys. Rev. D* **43**, 3895 (1991).
- [56] F. D. Ryan, Spinning boson stars with large self-interaction, *Phys. Rev. D* **55**, 6081 (1997).
- [57] F. S. Guzman, Evolving spherical boson stars on a 3-D Cartesian grid, *Phys. Rev. D* **70**, 044033 (2004).
- [58] D. G. Levkov, A. G. Panin, and I. I. Tkachev, Gravitational Bose-Einstein condensation in the kinetic regime, *Phys. Rev. Lett.* **121**, 151301 (2018).
- [59] J. Veltmaat, J. C. Niemeyer, and B. Schwabe, Formation and structure of ultralight bosonic dark matter halos, *Phys. Rev. D* **98**, 043509 (2018).
- [60] M. A. Amin and P. Mocz, Formation, gravitational clustering, and interactions of nonrelativistic solitons in an expanding universe, *Phys. Rev. D* **100**, 063507 (2019).
- [61] A. Arvanitaki, S. Dimopoulos, M. Galanis, L. Lehner, J. O. Thompson, and K. Van Tilburg, Large-misalignment mechanism for the formation of compact axion structures: Signatures from the QCD axion to fuzzy dark matter, *Phys. Rev. D* **101**, 083014 (2020).
- [62] A. Bernal and F. Siddhartha Guzman, Scalar field dark matter: Head-on interaction between two structures, *Phys. Rev. D* **74**, 103002 (2006).
- [63] C. Palenzuela, I. Olabarrieta, L. Lehner, and S. L. Liebling, Head-on collisions of boson stars, *Phys. Rev. D* **75**, 064005 (2007).
- [64] C. Palenzuela, L. Lehner, and S. L. Liebling, Orbital dynamics of binary boson star systems, *Phys. Rev. D* **77**, 044036 (2008).
- [65] M. W. Choptuik and F. Pretorius, Ultra relativistic particle collisions, *Phys. Rev. Lett.* **104**, 111101 (2010).
- [66] M. Bezares, C. Palenzuela, and C. Bona, Final fate of compact boson star mergers, *Phys. Rev. D* **95**, 124005 (2017).
- [67] C. Palenzuela, P. Pani, M. Bezares, V. Cardoso, L. Lehner, and S. Liebling, Gravitational wave signatures of highly compact boson star binaries, *Phys. Rev. D* **96**, 104058 (2017).
- [68] M. Bezares and C. Palenzuela, Gravitational waves from dark boson star binary mergers, *Classical Quantum Gravity* **35**, 234002 (2018).
- [69] T. Helfer, U. Sperhake, R. Croft, M. Radia, B.-X. Ge, and E. A. Lim, Malaise and remedy of binary boson-star initial data, *Classical Quantum Gravity* **39**, 074001 (2022).
- [70] M. Bezares, M. Bošković, S. Liebling, C. Palenzuela, P. Pani, and E. Barausse, Gravitational waves and kicks from the merger of unequal mass, highly compact boson stars, *Phys. Rev. D* **105**, 064067 (2022).
- [71] R. Croft, T. Helfer, B.-X. Ge, M. Radia, T. Evstafyeva, E. A. Lim, U. Sperhake, and K. Clough, The gravitational afterglow of boson stars, *Classical Quantum Gravity* **40**, 065001 (2023).
- [72] T. Evstafyeva, U. Sperhake, T. Helfer, R. Croft, M. Radia, B.-X. Ge, and E. A. Lim, Unequal-mass boson-star binaries: Initial data and merger dynamics, [arXiv:2212.08023](https://arxiv.org/abs/2212.08023).
- [73] N. Siemonsen and W. E. East, Binary boson stars: Merger dynamics and formation of rotating remnant stars, *Phys. Rev. D* **107**, 124018 (2023).
- [74] F. Di Giovanni, N. Sanchis-Gual, P. Cerdá-Durán, M. Zilhão, C. Herdeiro, J. A. Font, and E. Radu, Dynamical bar-mode instability in spinning bosonic stars, *Phys. Rev. D* **102**, 124009 (2020).
- [75] N. Siemonsen and W. E. East, Stability of rotating scalar boson stars with nonlinear interactions, *Phys. Rev. D* **103**, 044022 (2021).
- [76] F. E. Schunck and D. F. Torres, Boson stars with generic self-interactions, *Int. J. Mod. Phys. D* **09**, 601 (2000).
- [77] R. Friedberg, T. D. Lee, and Y. Pang, Scalar soliton stars and black holes, *Phys. Rev. D* **35**, 3658 (1987).
- [78] D. Guerra, C. F. B. Macedo, and P. Pani, Axion boson stars, *J. Cosmol. Astropart. Phys.* **09** (2019) 061; **06** (2020) E01.
- [79] C. A. R. Herdeiro, A. M. Pombo, and E. Radu, Asymptotically flat scalar, Dirac and Proca stars: Discrete vs. continuous families of solutions, *Phys. Lett. B* **773**, 654 (2017).
- [80] L. G. Collodel, B. Kleihaus, and J. Kunz, Excited boson stars, *Phys. Rev. D* **96**, 084066 (2017).
- [81] M. Bošković and E. Barausse, Soliton boson stars, Q-balls and the causal Buchdahl bound, *J. Cosmol. Astropart. Phys.* **02** (2022) 032.
- [82] L. G. Collodel and D. D. Doneva, Solitonic boson stars: Numerical solutions beyond the thin-wall approximation, *Phys. Rev. D* **106**, 084057 (2022).
- [83] A. M. Pombo, J. a. M. S. Oliveira, and N. M. Santos, Scalarocca stars: Coupled scalar-Proca solitons, *Phys. Rev. D* **108**, 044044 (2023).
- [84] F. H. Vincent, Z. Meliani, P. Grandclement, E.ourgoulhon, and O. Straub, Imaging a boson star at the Galactic center, *Classical Quantum Gravity* **33**, 105015 (2016).
- [85] P. V. P. Cunha, C. A. R. Herdeiro, E. Radu, and H. F. Runarsson, Shadows of Kerr black holes with scalar hair, *Phys. Rev. Lett.* **115**, 211102 (2015).



- [86] P. V. P. Cunha, J. Grover, C. Herdeiro, E. Radu, H. Runarsson, and A. Wittig, Chaotic lensing around boson stars and Kerr black holes with scalar hair, *Phys. Rev. D* **94**, 104023 (2016).
- [87] P. V. P. Cunha and C. A. R. Herdeiro, Shadows and strong gravitational lensing: A brief review, *Gen. Relativ. Gravit.* **50**, 42 (2018).
- [88] C. A. R. Herdeiro, A. M. Pombo, E. Radu, P. V. P. Cunha, and N. Sanchis-Gual, The imitation game: Proca stars that can mimic the Schwarzschild shadow, *J. Cosmol. Astropart. Phys.* **04** (2021) 051.
- [89] J. a. L. Rosa and D. Rubiera-Garcia, Shadows of boson and Proca stars with thin accretion disks, *Phys. Rev. D* **106**, 084004 (2022).
- [90] D. F. Torres, S. Capozziello, and G. Lambiase, A supermassive scalar star at the galactic center?, *Phys. Rev. D* **62**, 104012 (2000).
- [91] V. Diemer, K. Eilers, B. Hartmann, I. Schaffer, and C. Toma, Geodesic motion in the space-time of a noncompact boson star, *Phys. Rev. D* **88**, 044025 (2013).
- [92] Y. Brihaye, V. Diemer, and B. Hartmann, Charged Q-balls and boson stars and dynamics of charged test particles, *Phys. Rev. D* **89**, 084048 (2014).
- [93] A. M. Pombo and I. D. Saltas, A sun-like star orbiting a boson star, *Mon. Not. R. Astron. Soc.* **524**, 4083 (2023).
- [94] P. Grandclement, C. Somé, and E.ourgoulhon, Models of rotating boson stars and geodesics around them: New type of orbits, *Phys. Rev. D* **90**, 024068 (2014).
- [95] M. Grould, Z. Meliani, F. H. Vincent, P. Grandclément, and E.ourgoulhon, Comparing timelike geodesics around a Kerr black hole and a boson star, *Classical Quantum Gravity* **34**, 215007 (2017).
- [96] Y.-P. Zhang, Y.-B. Zeng, Y.-Q. Wang, S.-W. Wei, and Y.-X. Liu, Motion of test particle in rotating boson star, *Phys. Rev. D* **105**, 044021 (2022).
- [97] J. F. M. Delgado, C. A. R. Herdeiro, and E. Radu, EMRIs around  $j = 1$  black holes with synchronised hair, [arXiv:2305.02333](https://arxiv.org/abs/2305.02333).
- [98] C. A. R. Herdeiro and E. Radu, Kerr black holes with scalar hair, *Phys. Rev. Lett.* **112**, 221101 (2014).
- [99] L. G. Collodel, D. D. Doneva, and S. S. Yazadjiev, Equatorial extreme-mass-ratio inspirals in Kerr black holes with scalar hair spacetimes, *Phys. Rev. D* **105**, 044036 (2022).
- [100] Y.-P. Zhang, Y.-B. Zeng, Y.-Q. Wang, S.-W. Wei, P. A. Seoane, and Y.-X. Liu, Gravitational radiation pulses from extreme-mass-ratio-inspiral system with a supermassive boson star, [arXiv:2108.13170](https://arxiv.org/abs/2108.13170).
- [101] F. D. Ryan, Gravitational waves from the inspiral of a compact object into a massive, axisymmetric body with arbitrary multipole moments, *Phys. Rev. D* **52**, 5707 (1995).
- [102] F. D. Ryan, Accuracy of estimating the multipole moments of a massive body from the gravitational waves of a binary inspiral, *Phys. Rev. D* **56**, 1845 (1997).
- [103] F. D. Ryan, Scalar waves produced by a scalar charge orbiting a massive body with arbitrary multipole moments, *Phys. Rev. D* **56**, 7732 (1997).
- [104] M. Vaglio, C. Pacilio, A. Maselli, and P. Pani, Multipolar structure of rotating boson stars, *Phys. Rev. D* **105**, 124020 (2022).
- [105] T. A. Apostolatos, G. Lukes-Gerakopoulos, and G. Contopoulos, How to observe a non-Kerr spacetime using gravitational waves, *Phys. Rev. Lett.* **103**, 111101 (2009).
- [106] G. Lukes-Gerakopoulos, T. A. Apostolatos, and G. Contopoulos, Observable signature of a background deviating from the Kerr metric, *Phys. Rev. D* **81**, 124005 (2010).
- [107] G. Contopoulos, G. Lukes-Gerakopoulos, and T. A. Apostolatos, Orbits in a non-Kerr dynamical system, *Int. J. Bifurcation Chaos Appl. Sci. Eng.* **21**, 2261 (2011).
- [108] G. Lukes-Gerakopoulos, The non-integrability of the Zipoy-Voorhees metric, *Phys. Rev. D* **86**, 044013 (2012).
- [109] O. Zelenka and G. Lukes-Gerakopoulos, Chaotic motion in the Johannsen-Psaltis spacetime, in *Proceedings of the Workshop on Black Holes and Neutron Stars* (2017), [arXiv:1711.02442](https://arxiv.org/abs/1711.02442).
- [110] O. Zelenka, G. Lukes-Gerakopoulos, V. Witzany, and O. Kopáček, Growth of resonances and chaos for a spinning test particle in the Schwarzschild background, *Phys. Rev. D* **101**, 024037 (2020).
- [111] G. Lukes-Gerakopoulos and V. Witzany, Non-linear effects in EMRI dynamics and their imprints on gravitational waves, [arXiv:2103.06724](https://arxiv.org/abs/2103.06724).
- [112] K. Destounis, A. G. Suvorov, and K. D. Kokkotas, Testing spacetime symmetry through gravitational waves from extreme-mass-ratio inspirals, *Phys. Rev. D* **102**, 064041 (2020).
- [113] A. Deich, A. Cárdenas-Avendaño, and N. Yunes, Chaos in quadratic gravity, *Phys. Rev. D* **106**, 024040 (2022).
- [114] C.-Y. Chen, F.-L. Lin, and A. Patel, Resonant islands of effective-one-body dynamics, *Phys. Rev. D* **106**, 084064 (2022).
- [115] K. Destounis and K. D. Kokkotas, Slowly-rotating compact objects: The nonintegrability of Hartle-Thorne particle geodesics, [arXiv:2305.18522](https://arxiv.org/abs/2305.18522).
- [116] Z. Pan, H. Yang, L. Bernard, and B. Bonga, Resonant dynamics of extreme mass-ratio inspirals in a perturbed Kerr spacetime, [arXiv:2306.06576](https://arxiv.org/abs/2306.06576).
- [117] K. Destounis, A. G. Suvorov, and K. D. Kokkotas, Gravitational-wave glitches in chaotic extreme-mass-ratio inspirals, *Phys. Rev. Lett.* **126**, 141102 (2021).
- [118] K. Destounis and K. D. Kokkotas, Gravitational-wave glitches: Resonant islands and frequency jumps in non-integrable extreme-mass-ratio inspirals, *Phys. Rev. D* **104**, 064023 (2021).
- [119] K. Destounis, G. Huez, and K. D. Kokkotas, Geodesics and gravitational waves in chaotic extreme-mass-ratio inspirals: The curious case of Zipoy-Voorhees black-hole mimickers, *Gen. Relativ. Gravit.* **55**, 71 (2023).
- [120] K. Glampedakis, Extreme mass ratio inspirals: LISA's unique probe of black hole gravity, *Classical Quantum Gravity* **22**, S605 (2005).
- [121] P. Amaro-Seoane *et al.* (LISA Collaboration), Laser interferometer space antenna, [arXiv:1702.00786](https://arxiv.org/abs/1702.00786).
- [122] V. Baibhav *et al.*, Probing the nature of black holes: Deep in the mHz gravitational-wave sky, *Exp. Astron.* **51**, 1385 (2021).
- [123] P. Amaro-Seoane *et al.*, Astrophysics with the laser interferometer space antenna, *Living Rev. Relativity* **26**, 2 (2023).

- [124] K. G. Arun *et al.* (LISA Collaboration), New horizons for fundamental physics with LISA, *Living Rev. Relativity* **25**, 4 (2022).
- [125] N. Karnesis *et al.*, The laser interferometer space antenna mission in Greece white paper, [arXiv:2209.04358](https://arxiv.org/abs/2209.04358).
- [126] J. Luo *et al.* (TianQin Collaboration), TianQin: A spaceborne gravitational wave detector, *Classical Quantum Gravity* **33**, 035010 (2016).
- [127] W.-H. Ruan, Z.-K. Guo, R.-G. Cai, and Y.-Z. Zhang, Taiji program: Gravitational-wave sources, *Int. J. Mod. Phys. A* **35**, 2050075 (2020).
- [128] W.-H. Ruan, C. Liu, Z.-K. Guo, Y.-L. Wu, and R.-G. Cai, The LISA-Taiji network, *Nat. Astron.* **4**, 108 (2020).
- [129] S. Barsanti, V. De Luca, A. Maselli, and P. Pani, Detecting subsolar-mass primordial black holes in extreme mass-ratio inspirals with LISA and Einstein telescope, *Phys. Rev. Lett.* **128**, 111104 (2022).
- [130] R. H. Boyer and R. W. Lindquist, Maximal analytic extension of the Kerr metric, *J. Math. Phys. (N.Y.)* **8**, 265 (1967).
- [131] C. W. Misner, K. S. Thorne, and J. A. Wheeler, *Gravitation* (W. H. Freeman, San Francisco, 1973).
- [132] B. Carter, Global structure of the Kerr family of gravitational fields, *Phys. Rev.* **174**, 1559 (1968).
- [133] G. Contopoulos, *Order and Chaos in Dynamical Astronomy* (Springer-Verlag, New York, 2003).
- [134] D. M. Zipoy, Topology of some spheroidal metrics, *J. Math. Phys. (N.Y.)* **7**, 1137 (1966).
- [135] B. H. Voorhees, Static axially symmetric gravitational fields, *Phys. Rev. D* **2**, 2119 (1970).
- [136] V. Cardoso, K. Destounis, F. Duque, R. P. Macedo, and A. Maselli, Black holes in galaxies: Environmental impact on gravitational-wave generation and propagation, *Phys. Rev. D* **105**, L061501 (2022).
- [137] V. Cardoso, K. Destounis, F. Duque, R. Panosso Macedo, and A. Maselli, Gravitational waves from extreme-mass-ratio systems in astrophysical environments, *Phys. Rev. Lett.* **129**, 241103 (2022).
- [138] K. Destounis, A. Kulathingal, K. D. Kokkotas, and G. O. Papadopoulos, Gravitational-wave imprints of compact and galactic-scale environments in extreme-mass-ratio binaries, *Phys. Rev. D* **107**, 084027 (2023).
- [139] L. Polcar, G. Lukes-Gerakopoulos, and V. Witzany, Extreme mass ratio inspirals into black holes surrounded by matter, *Phys. Rev. D* **106**, 044069 (2022).
- [140] E. Figueiredo, A. Maselli, and V. Cardoso, Black holes surrounded by generic dark matter profiles: Appearance and gravitational-wave emission, *Phys. Rev. D* **107**, 104033 (2023).
- [141] J. B. Hartle and K. S. Thorne, Slowly rotating relativistic stars. II. Models for neutron stars and supermassive stars, *Astrophys. J.* **153**, 807 (1968).
- [142] V. S. Manko, E. W. Mielke, and J. D. Sanabria-Gomez, Exact solution for the exterior field of a rotating neutron star, *Phys. Rev. D* **61**, 081501 (2000).
- [143] G. Pappas and T. A. Apostolatos, An all-purpose metric for the exterior of any kind of rotating neutron star, *Mon. Not. R. Astron. Soc.* **429**, 3007 (2013).
- [144] G. Pappas, An accurate metric for the spacetime around rotating neutron stars, *Mon. Not. R. Astron. Soc.* **466**, 4381 (2017).
- [145] V. S. Manko and I. D. Novikov, Generalizations of the Kerr and Kerr-Newman metrics possessing an arbitrary set of mass-multipole moments, *Classical Quantum Gravity* **9**, 2477 (1992).
- [146] V. S. Manko, J. D. Sanabria-Gomez, and O. V. Manko, Nine parameter electrovac metric involving rational functions, *Phys. Rev. D* **62**, 044048 (2000).
- [147] N. A. Collins and S. A. Hughes, Towards a formalism for mapping the space-times of massive compact objects: Bumpy black holes and their orbits, *Phys. Rev. D* **69**, 124022 (2004).
- [148] K. Glampedakis and S. Babak, Mapping spacetimes with LISA: Inspiral of a test-body in a ‘quasi-Kerr’ field, *Classical Quantum Gravity* **23**, 4167 (2006).
- [149] S. J. Vigeland and S. A. Hughes, Spacetime and orbits of bumpy black holes, *Phys. Rev. D* **81**, 024030 (2010).
- [150] T. Johannsen and D. Psaltis, A metric for rapidly spinning black holes suitable for strong-field tests of the no-hair theorem, *Phys. Rev. D* **83**, 124015 (2011).
- [151] S. Vigeland, N. Yunes, and L. Stein, Bumpy black holes in alternate theories of gravity, *Phys. Rev. D* **83**, 104027 (2011).
- [152] T. Johannsen, A metric for testing the nature of black holes, *J. Phys. Conf. Ser.* **410**, 012136 (2013).
- [153] T. Johannsen, Regular black hole metric with three constants of motion, *Phys. Rev. D* **88**, 044002 (2013).
- [154] R. Emparan, P. Figueras, and M. Martínez, Bumpy black holes, *J. High Energy Phys.* **12** (2014) 072.
- [155] V. Cardoso, P. Pani, and J. Rico, On generic parametrizations of spinning black-hole geometries, *Phys. Rev. D* **89**, 064007 (2014).
- [156] L. Rezzolla and A. Zhidenko, New parametrization for spherically symmetric black holes in metric theories of gravity, *Phys. Rev. D* **90**, 084009 (2014).
- [157] R. Konoplya, L. Rezzolla, and A. Zhidenko, General parametrization of axisymmetric black holes in metric theories of gravity, *Phys. Rev. D* **93**, 064015 (2016).
- [158] C. J. Moore, A. J. K. Chua, and J. R. Gair, Gravitational waves from extreme mass ratio inspirals around bumpy black holes, *Classical Quantum Gravity* **34**, 195009 (2017).
- [159] E. E. Flanagan and T. Hinderer, Transient resonances in the inspirals of point particles into black holes, *Phys. Rev. Lett.* **109**, 071102 (2012).
- [160] C. P. L. Berry, R. H. Cole, P. Cañizares, and J. R. Gair, Importance of transient resonances in extreme-mass-ratio inspirals, *Phys. Rev. D* **94**, 124042 (2016).
- [161] L. Speri and J. R. Gair, Assessing the impact of transient orbital resonances, *Phys. Rev. D* **103**, 124032 (2021).
- [162] P. Gupta, L. Speri, B. Bonga, A. J. K. Chua, and T. Tanaka, Modeling transient resonances in extreme-mass-ratio inspirals, *Phys. Rev. D* **106**, 104001 (2022).
- [163] J. Möser, On invariant curves of area-preserving mappings of an annulus, *Nachr. Akad. Wiss. Goettingen II* **1**, 1 (1962).
- [164] V. I. Arnol’d, Proof of a theorem of A. N. Kolmogorov on the invariance of quasi-periodic motions under small perturbations of the Hamiltonian, *Russ. Math. Surv.* **18**, 9 (1963).

- [165] G. D. Birkhoff, Proof of Poincaré’s geometric theorem, *Trans. Am. Math. Soc.* **14**, 14 (1913).
- [166] U. Ruangsri and S. A. Hughes, Census of transient orbital resonances encountered during binary inspiral, *Phys. Rev. D* **89**, 084036 (2014).
- [167] L. Barack, Gravitational self-force in extreme mass-ratio inspirals, *Classical Quantum Gravity* **26**, 213001 (2009).
- [168] F. E. Schunck and E. W. Mielke, Rotating boson stars, in *Relativity and Scientific Computing: Computer Algebra, Numerics, Visualization*, edited by F. W. Hehl, R. A. Puntigam, and H. Ruder (Springer Berlin Heidelberg, Berlin, Heidelberg, 1996), pp. 138–151.
- [169] S. Yoshida and Y. Eriguchi, Rotating boson stars in general relativity, *Phys. Rev. D* **56**, 762 (1997).
- [170] P. Amaro-Seoane, J. Barranco, A. Bernal, and L. Rezzolla, Constraining scalar fields with stellar kinematics and collisional dark matter, *J. Cosmol. Astropart. Phys.* **11** (2010) 002.
- [171] R. Brito, V. Cardoso, C. A. R. Herdeiro, and E. Radu, Proca stars: Gravitating Bose–Einstein condensates of massive spin 1 particles, *Phys. Lett. B* **752**, 291 (2016).
- [172] C. Herdeiro and E. Radu, Construction and physical properties of Kerr black holes with scalar hair, *Classical Quantum Gravity* **32**, 144001 (2015).
- [173] P. V. P. Cunha, C. Herdeiro, E. Radu, and N. Sanchis-Gual, Exotic compact objects and the fate of the light-ring instability, *Phys. Rev. Lett.* **130**, 061401 (2023).
- [174] N. Franchini, P. Pani, A. Maselli, L. Gualtieri, C. A. R. Herdeiro, E. Radu, and V. Ferrari, Constraining black holes with light boson hair and boson stars using epicyclic frequencies and quasiperiodic oscillations, *Phys. Rev. D* **95**, 124025 (2017).
- [175] A. Pound and B. Wardell, Black hole perturbation theory and gravitational self-force, in *Handbook of Gravitational Wave Astronomy*, edited by C. Bambi, S. Katsanevas, and K. D. Kokkotas (Springer, Singapore, 2021), 10.1007/978-981-15-4702-7\_38-1.
- [176] M. van de Meent, Gravitational self-force on eccentric equatorial orbits around a Kerr black hole, *Phys. Rev. D* **94**, 044034 (2016).
- [177] M. van de Meent, Gravitational self-force on generic bound geodesics in Kerr spacetime, *Phys. Rev. D* **97**, 104033 (2018).
- [178] A. Pound, Nonlinear gravitational self-force: Second-order equation of motion, *Phys. Rev. D* **95**, 104056 (2017).
- [179] S. A. Teukolsky, Perturbations of a rotating black hole. I. Fundamental equations for gravitational, electromagnetic, and neutrino-field perturbations, *Astrophys. J.* **185**, 635 (1973).
- [180] S. A. Teukolsky and W. H. Press, Perturbations of a rotating black hole. III—Interaction of the hole with gravitational and electromagnetic IC radiation, *Astrophys. J.* **193**, 443 (1974).
- [181] S. L. Detweiler, Black holes and gravitational waves. I. Circular orbits about a rotating hole, *Astrophys. J.* **225**, 687 (1978).
- [182] M. Sasaki and T. Nakamura, Gravitational radiation from a Kerr black hole. I. Formulation and a method for numerical analysis, *Prog. Theor. Phys.* **67**, 1788 (1982).
- [183] Y. Mino, M. Sasaki, M. Shibata, H. Tagoshi, and T. Tanaka, Black hole perturbation: Chapter 1, *Prog. Theor. Phys. Suppl.* **128**, 1 (1997).
- [184] S. A. Hughes, The evolution of circular, nonequatorial orbits of Kerr black holes due to gravitational wave emission, *Phys. Rev. D* **61**, 084004 (2000); **63**, 049902(E) (2001); **65**, 069902(E) (2002); **67**, 089901(E) (2003); **78**, 109902(E) (2008); **90**, 109904(E) (2014).
- [185] S. A. Hughes, Evolution of circular, nonequatorial orbits of Kerr black holes due to gravitational wave emission. II. Inspiral trajectories and gravitational wave forms, *Phys. Rev. D* **64**, 064004 (2001); **88**, 109902(E) (2013).
- [186] S. Drasco and S. A. Hughes, Gravitational wave snapshots of generic extreme mass ratio inspirals, *Phys. Rev. D* **73**, 024027 (2006); **88**, 109905(E) (2013); **90**, 109905(E) (2014).
- [187] E. Poisson, Absorption of mass and angular momentum by a black hole: Time-domain formalisms for gravitational perturbations, and the small-hole / slow-motion approximation, *Phys. Rev. D* **70**, 084044 (2004).
- [188] K. Martel, Gravitational wave forms from a point particle orbiting a Schwarzschild black hole, *Phys. Rev. D* **69**, 044025 (2004).
- [189] R. Lopez-Aleman, G. Khanna, and J. Pullin, Perturbative evolution of particle orbits around Kerr black holes: Time domain calculation, *Classical Quantum Gravity* **20**, 3259 (2003).
- [190] G. Khanna, Teukolsky evolution of particle orbits around Kerr black holes in the time domain: Elliptic and inclined orbits, *Phys. Rev. D* **69**, 024016 (2004).
- [191] A. Pound, Second-order gravitational self-force, *Phys. Rev. Lett.* **109**, 051101 (2012).
- [192] A. Pound, B. Wardell, N. Warburton, and J. Miller, Second-order self-force calculation of gravitational binding energy in compact binaries, *Phys. Rev. Lett.* **124**, 021101 (2020).
- [193] A. Spiers, Second-order gravitational self-force in Kerr spacetime, Doctoral Thesis, University of Southampton, 2022.
- [194] K. Glampedakis, S. A. Hughes, and D. Kennefick, Approximating the inspiral of test bodies into Kerr black holes, *Phys. Rev. D* **66**, 064005 (2002).
- [195] J. R. Gair and K. Glampedakis, Improved approximate inspirals of test-bodies into Kerr black holes, *Phys. Rev. D* **73**, 064037 (2006).
- [196] R. Ruffini and M. Sasaki, On a semi-relativistic treatment of the gravitational radiation from a mass thrust into a black hole, *Prog. Theor. Phys.* **66**, 1627 (1981).
- [197] M. Sasaki, On the generation mechanism of gravitational waves in the vicinity of a black hole, *Prog. Theor. Phys.* **69**, 815 (1983).
- [198] S. Babak, H. Fang, J. R. Gair, K. Glampedakis, and S. A. Hughes, ‘Kludge’ gravitational waveforms for a test-body orbiting a Kerr black hole, *Phys. Rev. D* **75**, 024005 (2007); **77**, 04990(E) (2008).
- [199] K. Glampedakis and D. Kennefick, Zoom and whirl: Eccentric equatorial orbits around spinning black holes and their evolution under gravitational radiation reaction, *Phys. Rev. D* **66**, 044002 (2002).

- [200] L. Barack and C. Cutler, Using LISA EMRI sources to test off-Kerr deviations in the geometry of massive black holes, *Phys. Rev. D* **75**, 042003 (2007).
- [201] J. R. Gair, C. Li, and I. Mandel, Observable properties of orbits in exact bumpy spacetimes, *Phys. Rev. D* **77**, 024035 (2008).
- [202] S. Mukherjee, O. Kopacek, and G. Lukes-Gerakopoulos, Resonance crossing of a charged body in a magnetized Kerr background: An analog of extreme mass ratio inspiral, *Phys. Rev. D* **107**, 064005 (2023).
- [203] P. Canizares, J. R. Gair, and C. F. Sopuerta, Testing Chern-Simons modified gravity with gravitational-wave detections of extreme-mass-ratio binaries, *Phys. Rev. D* **86**, 044010 (2012).
- [204] C. Cutler, Angular resolution of the LISA gravitational wave detector, *Phys. Rev. D* **57**, 7089 (1998).
- [205] L. Barack and C. Cutler, LISA capture sources: Approximate waveforms, signal-to-noise ratios, and parameter estimation accuracy, *Phys. Rev. D* **69**, 082005 (2004).
- [206] M. van de Meent, Conditions for sustained orbital resonances in extreme mass ratio inspirals, *Phys. Rev. D* **89**, 084033 (2014).
- [207] K. Kiuchi and K.-i. Maeda, Gravitational waves from chaotic dynamical system, *Phys. Rev. D* **70**, 064036 (2004).
- [208] G. A. Piovano, A. Maselli, and P. Pani, Extreme mass ratio inspirals with spinning secondary: A detailed study of equatorial circular motion, *Phys. Rev. D* **102**, 024041 (2020).
- [209] I. Bena, E. J. Martinec, S. D. Mathur, and N. P. Warner, Snowmass white paper: Micro- and macro-structure of black holes, [arXiv:2203.04981](https://arxiv.org/abs/2203.04981).
- [210] I. Bena and D. R. Mayerson, Multipole ratios: A new window into black holes, *Phys. Rev. Lett.* **125**, 221602 (2020).
- [211] M. Bianchi, D. Consoli, A. Grillo, J. F. Morales, P. Pani, and G. Raposo, Distinguishing fuzzballs from black holes through their multipolar structure, *Phys. Rev. Lett.* **125**, 221601 (2020).
- [212] I. Bena and D. R. Mayerson, Black holes lessons from multipole ratios, *J. High Energy Phys.* **03** (2021) 114.
- [213] M. Bianchi, D. Consoli, A. Grillo, J. F. Morales, P. Pani, and G. Raposo, The multipolar structure of fuzzballs, *J. High Energy Phys.* **01** (2021) 003.
- [214] K. Fransen and D. R. Mayerson, Detecting equatorial symmetry breaking with LISA, *Phys. Rev. D* **106**, 064035 (2022).